CHARGE AND SPIN TRANSPORT IN COMPLEX SYSTEMS ASSOCIATED WITH SPINTRONICS

By

YE XIONG

Bachelor of Science in Physics

Nanjing University

China

1998

Submitted to the Faculty of the
Graduate College of the
Oklahoma State University
in partial fulfillment of
the requirements for
the Degree of
DOCTOR OF PHILOSOPHY
December, 2005

CHARGE AND SPIN TRANSPORT IN COMPLEX

SYSTEMS ASSOCIATED WITH

SPINTRONICS

Thesis Approved:

XINCHENG XIE

Thesis Adviser

JOHN MINTMIRE

PAUL A. WESTHAUS

WEILI ZHANG

A. GORDON EMSLIE

Dean of the Graduate College

ACKNOWLEDGMENTS

I wish to express my sincere gratitude to my advisor Prof. Xincheng Xie for his intelligent supervision, constructive guidance and inspiration. My appreciation extends to my other committee members Prof. Paul A. Westhaus, Prof. John Mintmire and Prof. Weili Zhang.

More over, I wish to express my appreciation to my parent for their constant support.

I would also like to thank all my friends.

TABLE OF CONTENTS

LIST OF TABLES

Table Page

LIST OF FIGURES

CHAPTER 1

INTRODUCTION

ABSTRACT: A brief report on charge and spin transport in quantum system is given in this chapter. With the advance of modern semiconductor technology, a new class of devices whose principle is associated with electron's spin degree of freedom has emerged. The studies of these devices has formed a completely new branch of electronics, called "spintronics".

1.1 Publication list

- Spin Entanglement and '0.7 Anomaly' in Quantum Point Contact, Ye Xiong, Shi-Jie Xiong and X.C. Xie, (submitted to Phys. Rev. Lett.).

- Low-Temperature Saturation of Variable-Range Hopping and Delocalization of Electron States by Entanglement with Phonons in Two Dimensions, Ye Xiong, X.C. Xie, and Shi-Jie Xiong, Phys. Rev. B 67, 140201 Rapid Communications (2003).

- Crossover from Insulator to Metallic-like State in Silicon Inversion Layers and GaAs Quantum Wells, Shi-Jie Xiong, Ye Xiong and S. N. Evangelou, Phys. Lett. A 305, 437 (2002).

- Percolative Conductivity and Critical Exponents in Mixed-Valent Manganites, Ye Xiong, Shun-Qing Shen, and X.C. Xie, Phys. Rev. B 63, 140418 Rapid Communications (2001).

- Localization Effect of Ordered and Disordered Orbital Polarization in a Simplified Double-Exchange Model, Ye Xiong, Shi-Jie Xiong, and D.Y. Xing, Phys. Rev. B 61, 11240 Brief Reports (2000).

- Resonant Transmission through a Quantum Dot in the Coulomb Blockade Regime, Shi-Jie Xiong and Ye Xiong, Phys. Rev. Lett. 83, 1407 (1999).

- Correlation between the phase of transmission resonances and parity of bound states in a quantum dot, Tao Chen, Ye Xiong, and Shi-Jie Xiong, Journal of Physics - Condensed Matter 12, 4959 (2000).

In this thesis, the problems on charge and spin transport in several complex systems associated with spintronics are explored. With the benefit of modern semiconductor technology, a new class of devices whose principle is associated with the spin degree of freedom has emerged. The study of such devices forms a completely new branch of electronics, called "spintronics". As the operating principle of spintronics devices is different from the ordinary electronics devices, it is necessary to understand the basic rules which govern the transport of charge and spin degrees in relevant degrees. Being interested in these problems, I have carried out the following investigations:

(1) Recent experiments have shown that some colossal magnetoresistance (CMR) materials exhibit percolation transition. However, the conductivity exponent deviates substantially from the value of conventional percolation theory. In particular, the exponent varies roughly by a factor of 3 with or without external magnetic field. To understand this exponent discrepancy, we carried out theoretical studies using real-space-renormalization method and numerical calculations. Our results are in good agreement with some experimental findings.

(2) We investigate low temperature transport properties in a two dimensional electronic system coupled with phonons. It is found that some of the localized states will be delocalized by the entanglement with phonons even when the temperature approaches absolute zero. The distribution of phonons near zero temperature depart from the Boson distribution because the entangled states are preferred from the energy point of view. This leads to the low-temperature saturation of the variable range hopping of electrons and the existence of a metal-like behavior in two dimensions.

(3) Spin entanglement between itinerant and localized electrons in a short one-dimensional chain with low Fermi energy and its effect on transport properties are investigated. As long as the entanglement between itinerant and localized electrons is maintained, a $\frac{3}{4}$ quantum conductance occurs due to the blockade for the singlet state but no effect on the triplets. This will result in an observation of conductance near

"0.7". We find that this blockade effect is complete as the effective coupling between itinerate and localized electrons exceeding a threshold. The many-body correlation of electrons near the band edge reduces this accessibility at low temperature and causes specific temperature dependence of the conductance. These results provide a natural explanation for the "0.7 anomaly" in quantum point contacts.

In the past few decades, the development of solid state physics has enabled physicists to design abundant semiconductor devices. Despite the advantage of these quantum devices, a principal quantum aspect of electron, its spin has been ignored. In recent years, however, a new class of devices whose principle is associated with the spin degree of freedom has emerged. The study of such devices forms a completely new branch of electronics, called "spintronics".

The first breakthrough of "spintronics" happened 20 years ago on giant magnetoresistance (GMR). Because the spin degree of freedom is not isolated, it can interact with external magnetic field and orbital motion of electron itself. As transmitting through an interface between two metals (or metallic grains) in different magnetized states, the spin state of the carrier can greatly affect the resultant transport properties. With applying an external magnetic field, the magnetic states of metals (or metallic grains) are altered, changing the spin state of the carrier situated in them. As a result the resistance of GMR materials can span over 2 order of magnitude with the application of external magnetic field. After ten years of development, the technology of GMR is matured and GMR materials begin to be applied in manufacture of devices such as hard disk headers.

As mentioned above, the coupling between spin and charge can create a new sort of functionality to the change of external field. The new devices that employ the functionality will operate on both charge and spin degrees of freedom, rather than on only one. Compared with the traditional "electronic" devices, the new "spintronic" devices exhibit many advantages, such as the high speed of data processing, the

integration of data processing and storage, the less power consumption, and the non-volatility. Moreover, as many experimental investigations have confirmed, in most nanostructures the environmental fluctuations have less effect on the spin degree of freedom than on the charge. Thus, the quantum information stored in spin state is easier to survive than stored in typical charge state. This makes the "spintronic" devices to be an ideal candidate of constructing quantum bits (qubits), which are basic logical units of the next generation of computer, the quantum computer.

Spintronics is still in the stage of rapid development. In the present time there exist several basic questions which must be answered before the industrial applications. Some of these questions are: What type of materials is mostly suitable to host operations of spin degree of freedom? How can experimentist prepare a designed spin state in a device? How can the spin state be processed? And finally, how the results of operations on spin states can be measured or read-out? In this work, I will focus on some topics that are related to the first two questions.

1.2 Diluted magnetic semiconductors - candidate materials suitable for hosting operations of spins

It is well-known that the semiconductors are very suitable for processing of the charge degree of freedom, but they can not host operations of spin states because the magnetic moments are absent. Physicists used to anticipate that some chemical compounds of magnetic elements, e.g., EuO, could be a bridge between ferromagnetism and semiconductor[1]. However, these compounds are difficult for single-crystallization and their Curie temperature T_c for ferromagnetism are usually low. Recently, some physicists turn attention back to semiconductors, because these materials are understood very well at least in the aspect of the charge motion, and lots of methods and technologies have been developed to manipulate spin degree of

freedom in semiconductors. One of these methods is to dope magnetic ions into semiconductors.

Owing to the development of low-temperature molecular beam epitaxy (LT-MBE) method[2], a kind of magnetic semiconductors called diluted magnetic semiconductors is available now. Diluted magnetic semiconductors (DMS), as the name indicates, are based on non-magnetic semiconductors alloyed with magnetic element. Usually the percentage of the magnetic element in a DMS is less than 20%. The recent discovery of ferromagnetism in $III-V$ based DMS's has generated great interest[3]. The understanding of the mechanism of this ferromagnetism becomes an important issue in this field.

1.3 Mean-field explanation of ferromagnetism in DMS

There are two subsystems in a DMS[4]: the magnetic moments localized in the doped magnetic ions and the itinerant carriers moving in the semiconductor. These two subsystems are interacted with each other by a Hund's exchange energy J_H. This interaction trends to align the spin of a carrier and the magnetic moment of an ion at one position to one direction ($J_H < 0$) or to the opposite direction ($J_H > 0$). Ferromagnetism occurs if the average value of all magnetic moments, the magnetization M, is nonzero in the absence of external magnetic field. Otherwise the phase of the system is paramagnetic. Two spin subbands of carriers will split under a finite magnetization M. Therefore, the free energy of the carrier subsystem is reduced by this splitting. The amount of this reduction of free energy can be expressed as

$$\Delta F = \frac{\chi_c}{2} H^2 = \frac{\chi_c}{2\chi_M^2} M^2, \tag{1.1}$$

where H is the magnetic field including the external one and that produced by the moments, χ_c and χ_M are susceptibility of itinerant carriers and local moments, respectively. Free-electron model gives $\chi_c = \frac{(\chi_M J_H)^2 \rho(E_F)}{4(g\mu_B)^2}$, where $\rho(E_F)$ is the density of states at Fermi surface E_F, g is the g-factor, and μ_B is the Bohr magneton.

Ignoring the interaction between magnetic atoms, the magnetization M will enhance the free energy of local magnetic atoms subsystem by

$$\Delta F_M = \frac{1}{2\chi_M} M^2. \tag{1.2}$$

In the standard Curie form, $\chi_M = \frac{Ng^2\mu_B^2 S(S+1)}{3kT}$, where N is the density of cation sites and $S = \frac{5}{2}$ for Mn.

The total change of free energy of the system is

$$\Delta F_{total} = \Delta F_M - \Delta F. \tag{1.3}$$

At Curie temperature T_c, the two free energy changes balance and the the further reduction of temperature gives rise to a spontaneous polarization M. From this one can determine the Curie temperature,

$$T_C = \frac{NS(S+1)\rho(E_F)\alpha^2}{12k}. \tag{1.4}$$

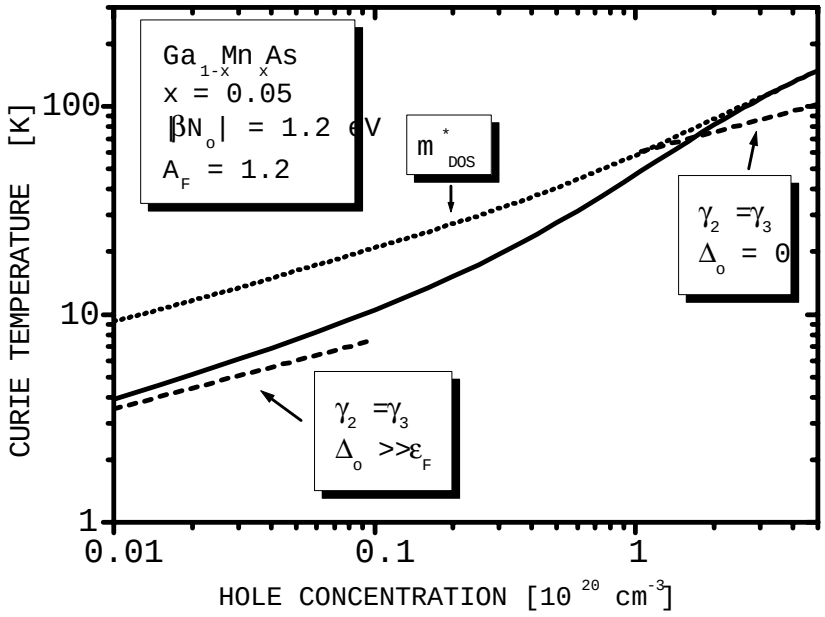

Figure 1.1. The calculated T_c versus the hole concentration for Mn-doped GaAs.

The calculated T_c as a function of the hole concentration for Mn doped GaAs is shown in Fig. 1.3, which is in good agreement with the experimental data. In Fig.

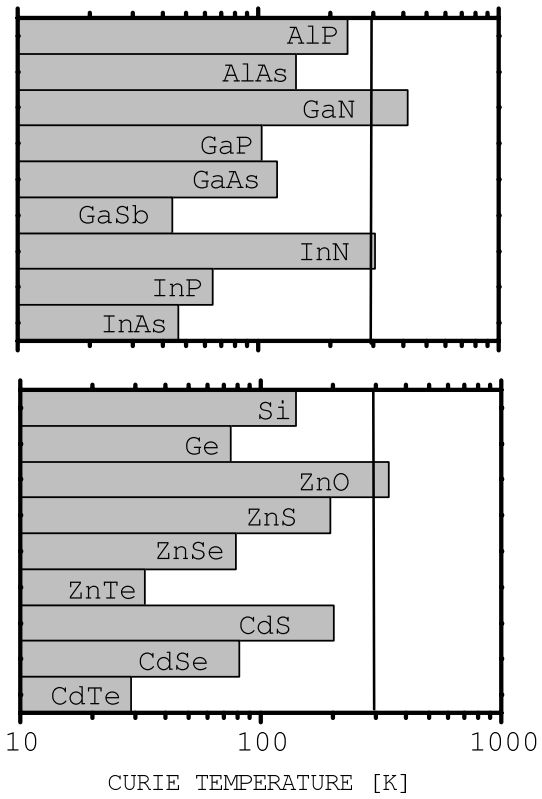

Figure 1.2. Curie temperatures evaluated for various $III - V$ (top panel) as well as $II - VI$ (bottom panel) DMS's containing 5% Mn.

1.3 the Curie temperature of various $III-V$ and $II-VI$ DMS's containing 5% Mn ions is shown.

1.4 Spin injection

When a device is connected to two electrodes, a charge current can be driven by a bias voltage which generates a inclined of Fermi energy between source and drain. The spin current $\vec{I}_{spin} = n_\uparrow \vec{v}_\uparrow - n_\downarrow \vec{v}_\downarrow$ vanishes in this case because the populations of carriers with spin up $\uparrow$ and spin down $\downarrow$ are the same and carriers with both spins are moving with the same average velocity.

One way to generate spin current is to manipulate the populations of carriers with different spins to be unbalanced in the electrodes, $n_\uparrow \neq n_\downarrow$. Another way is to make $\vec{v}_\uparrow \neq \vec{v}_\downarrow$.

In ferromagnetic materials, the two spin subbands are split by the Zeeman energy. When the Zeeman splitting is larger than the Fermi energy E_F, the Fermi surface might fall into a gap of one spin subband whereas the other spin subband is still metallic. The current flowing out of this spin polarized reservoir is of course spin polarized. Taking into account the mismatch in conductivity between the spin polarized current. A typical spin-injection setup is like this[5]: Current acquires a spin polarization within a ferromagnetic source electrode. This spin-polarized current flows into the nonmagnetic semiconductor and the spin of transmitted carriers relaxes at the rate $1/\tau_s$, where τ_s represents the relaxation time in the spin-flip scattering process of the material. If the distance between the source and drain is less than the typical length for spin relaxation, a spin polarized current is generated.

Taking into account the mismatch in conductivity between the semiconductor and the ferromagnetic source, G. Schmidt has derived the spin polarization rate α in the semiconductor[6]

$$\alpha = \frac{2\beta m}{(2m+1) - \beta^2}, \tag{1.5}$$

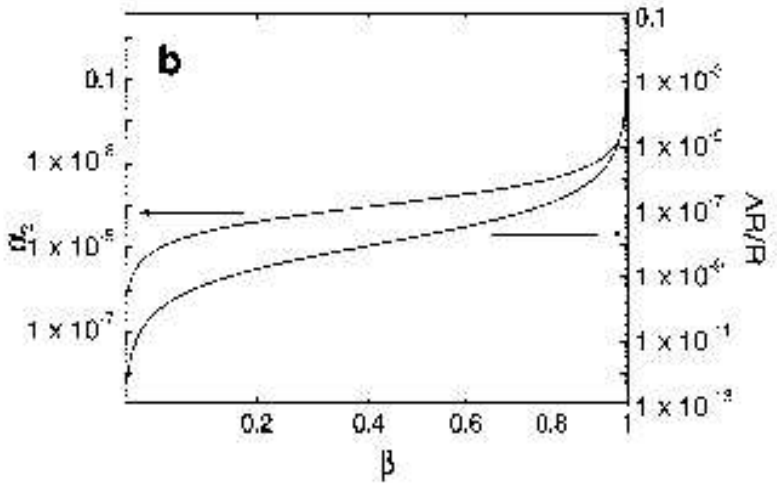

Figure 1.3. Dependence of spin polarization rate on β.

where β is the spin polarization in the bulk ferromagnet, and $m = \frac{\lambda_f \sigma}{\sigma_{fm} d}$, with λ_f being the spin scattering length in the ferromagnet, d the length of the system, σ and σ_{fm} the conductivities of the semiconductor and the ferromagnet, respectively.

As shown in fig. 1.3, α is not linearly related to β. An efficient spin injection requires the sufficiently high spin polarization in the ferromagnet. Fortunately, the $II - VI$ DMS is an ideal candidate. The giant Zeeman splitting is of the order of 100meV in the valence band and 20meV in the conduction band in Zn_{1-x} Mn_xSe[7], so it is very suitable for the spin injection.

CHAPTER 2

Percolative conductivity and critical exponents in mixed-valent manganites

ABSTRACT: Recent experiments have shown that some colossal magnetoresistance (CMR) materials exhibit a percolation transition. The conductivity exponent varies substantially with or without an external magnetic field. This finding prompted us to carry out theoretical studies of percolation transition in CMR systems. We find that the percolation transition coincides with the magnetic transition and this causes a large effect of a magnetic field on the percolation transition. Using real-space renormalization method and numerical calculations for two-dimensional (2D) and three-dimensional (3D) models, we obtain the conductivity exponent t to be 5.3 (3D) and 3.3 (2D) without a magnetic field, and 1.7 (3D) and 1.4 (2D) with a magnetic field.

2.1 Exponent discrepancy observed in CMR materials

Colossal magnetoresistance (CMR), an unusual large change of resistivity in the presence of a magnetic field, has been extensively studied in ferromagnetic perovskite manganites.[8] It is well known that the electronic phase diagrams of CMR materials are very complex. There are various ordering states and phase transitions as the carrier concentration is varied. For example, $La_{1-x}Ca_xMnO_3$, a typical double exchange ferromagnetic metal when x=0.33, becomes a charge ordered insulator with a specific type of electronic orbital and magnetic orderings when x=1/2. [9] Recently, it was demonstrated that $La_{1-x-y}Pr_yCa_xMnO_3$ (x=3/8) system, where Pr is chosen to vary the chemical pressure, may be electronically phase separated into a sub-micrometer-scale mixture of insulating regions and ferromagnetic (FM) metallic regions.[10, 11] Experimental findings of FM clusters and phase separation in CMR materials have also been reported in early studies.[12] Electron diffraction and dark-field imaging on the $La_{1-x-y}Pr_yCa_xMnO_3$ samples indicate that the insulating region is a x=1/2 charge ordered phase. This is not a charge congregation type of phase separation, which was observed in slightly doped antiferromagnetic manganites [13] and was extensively discussed. [14] CMR effect was observed in different samples with $0.275 < y < 0.41$, and was explained by percolative transport through the ferromagnetic domains. According to the percolation theory, the conductivity $\sigma \propto (p - p_0)^t$, where p is the concentration of the metallic phase and p_0 is its critical value. In Ref.[10], the exponent was studied in the presence and absence of an external magnetic field and two values are substantially different. Thus, the experiment shows that the percolative transport in the CMR systems depends sensitively on the relative spin orientation of adjacent ferromagnetic domains which is controlled by an applied magnetic field. The goal of this work is to develop a percolation theory which takes into account the magnetic transition in the CMR materials. In particular, we

would like to understand what causes the exponent to be so different with or without an external magnetic field.

2.2 Percolation model

Based on phenomenological considerations, we study two- or three-dimensional (2D or 3D) lattice percolation models. The conductivity and its critical exponent are calculated by means of real space renormalization and numerical methods. The system consists of three types of lattice sites. Each site has spin $S_i(= \pm 1, 0)$ where i denotes the index of a site. This model is similar to the site-diluted spin system used in Ref. [15]. $S_i = 0$ implies that the site is empty, meaning occupied by the x=1/2 charge ordered phase. $S_i = \pm 1$ means the site is occupied by the ferromagnetic metallic phase with up and down magnetizations.[16] The Hamiltonian of the spin interaction is Ising-like and is written as

$$H_s = -J \sum_{\langle i,j \rangle} S_i \cdot S_j + \sum_i H \cdot S_i. \tag{2.1}$$

Here $\langle i, j \rangle$ denotes a pair of the nearest neighbor sites, J is the interaction energy, and H is the strength of the external magnetic field. We consider a ferromagnetic interaction, i.e., $J > 0$. In order to investigate transport properties, we assume that the local conductivity between two nearest occupied sites is either 0 for antiparallel spins ($\uparrow\downarrow$ and $\downarrow\uparrow$) or 1 for parallel spins ($\uparrow\uparrow$ and $\downarrow\downarrow$) and is zero if one or both sites are empty. Thus, the conductivity between neighboring sites can be expressed as follows

$$\sigma_{ij} = \begin{cases} 1 & S_i \cdot S_j = 1 \\ 0 & \text{otherwise.} \end{cases} \tag{2.2}$$

2.3 Numerical results

First, we use the standard Monte-Carlo method to study the magnetic properties of the model. Knowing the spin structure is necessary for the transport studies

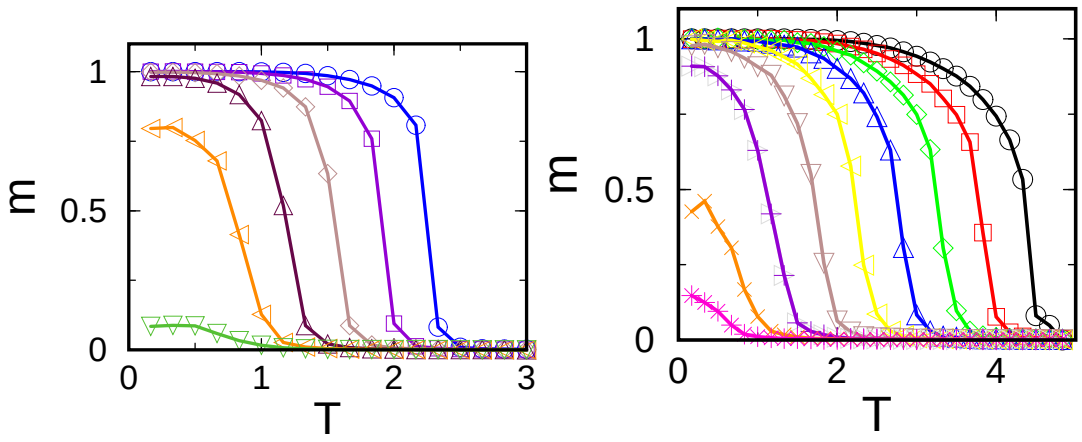

Figure 2.1. (a)The normalized spontaneous magnetization m' as a function of temperature T for different concentration p in the 2D model. From top to bottom, the concentrations are $p = 1.0$, 0.9, 0.8, 0.7, 0.6 and 0.5 The spin interactive strength J is taken as unity 1. The calculation is performed on 1000 samples whose size is 100×100. (b) m' as a function of T in the 3D model. The calculation is performed on 200 samples whose size is $10 \times 10 \times 10$. From top to bottom, the concentrations are $p = 1.0$, 0.9, 0.8, 0.7, 0.6, 0.5, 0.4, 0.3 and 0.2.

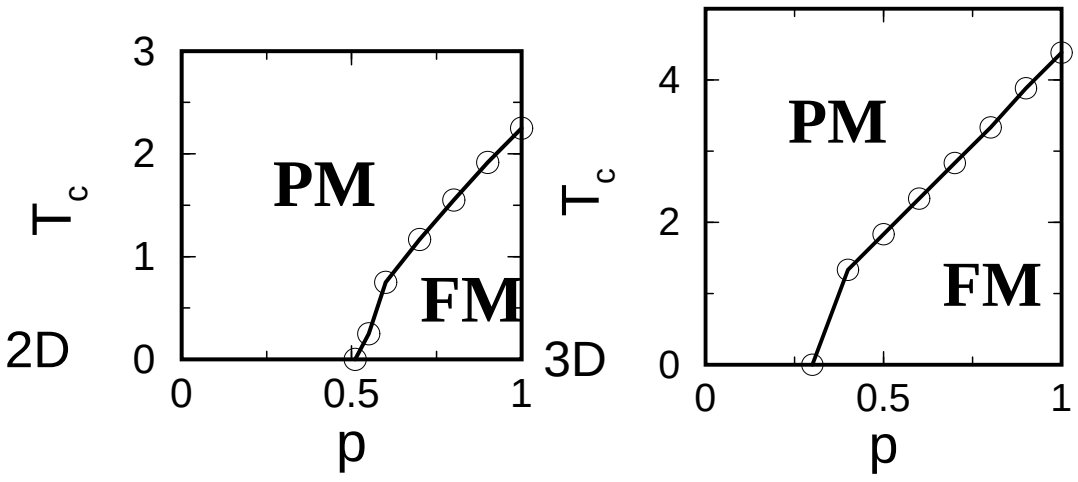

Figure 2.2. (a) The critical temperature T_c' as a function of the concentration p in the 2D case obtained from the data of Fig. 2.3 (a). (b) The critical temperature T_c' as a function of the concentration p in the 3D case obtained from the data of Fig. 2.3(b).

since the local conductivity depends on the spins. The conductance calculation is performed on a set of spin configurations produced by the Markov chain. In the Markov chain every spin configuration is generated from the previous one by using the probability $e^{-\beta\Delta H_s}/(e^{-\beta\Delta H_s}+1)$, where ΔH_s is the energy difference between these two configurations and $\beta = 1/k_BT$.[18] The calculations are carried out on finite square and cubic lattices for 2D and 3D systems and the periodic boundary condition is adopted to eliminate the boundary effects. The conductance G for every spin configuration in the Markov chain is obtained by calculating the total conductance of the resistor network.[17] In the resistor network, the local conductivity between neighboring sites is determined by Eq.2.2 The total conductance is calculated for many samples to obtain the average conductance.

When the charge order (CO) phase is dominant in some of the CMR materials, most sites are empty according to our model. Thus, most of the conductivities between neighboring sites are zero, corresponding to the low concentration limit ($p \sim 0$)

in the percolation model, where p is the probability of non-zero local conductivity. The small FM islands is well separated by the CO phase. Because the spin correlations between FM blocks are cut off by the CO phase, the spin orientation for each FM block is random, either up or down. Therefore, the spontaneous magnetization m will be zero at any temperature T. As p increases, m continues to be zero until p reaches p_0 at which the first infinite FM cluster appears. If $p > p_0$, a finite spontaneous magnetization appears for $T < T_c(p)$ with $T_c(p)$ the critical temperature at concentration p. In Figs. 2.3(a) and 2.3(b) we plot the normalized magnetization m as a function of temperature T with different concentration probabilities p for 2D and 3D systems, respectively, calculated using the Monte Carlo method. The interaction strength J is set to unity. It can be seen that when the temperature increases m is reduced and reaches zero at $T_c(p)$. From magnetization data with different size samples and through finite-size scaling, we can determine the critical temperature. In Figs. 2.3(a) and 2.3(b) we plot the relation between the critical temperature $T_c(p)$ and the concentration p. As shown in these plots, $T_c(p)$ will approach the Curie temperature T_c for the regular Ising model as p approaches to 1. We find that T_c determined from Fig.2.3 is $2.3J$ or $4.4J$ for 2D or 3D system. Both of them are in good agreement with the values of the regular Ising model.[19]

From the spin configurations of the system, we can calculate the conductance by using the local conductivity defined in Eq. (2.2). In a paramagnetic phase, there is no infinite cluster with spins pointing in the same direction. Hence, according to Eq. (2.2) there is no conducting path throughout the sample. On the other hand, the first conducting path appears simultaneously when the magnetization starts becoming non-zero. Thus, the phase transition from the FM phase to the paramagnetic phase is accompanied by the metal-insulator (MI) transition in the conductance. This implies that at zero temperature the MI transition occurs at the critical concentration of the percolation threshold p_0. Near the critical point the averaged conductance G can be

expressed as $G \sim (p - p_0)^t$, where t is the the conductance critical exponent for the transition.

2.4 Real space renormalization method

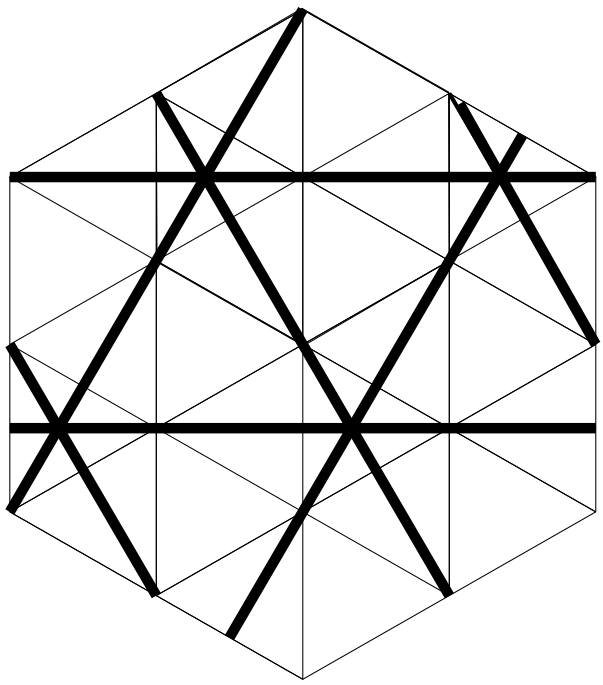

Figure 2.3. The illustration of renormalization in 2d triangle lattice

We now discuss the real space renormalization method. We start with a 2D system and later extend to a more complicated 3D system. The essential physics does not depend on dimensionality, although numerical numbers do. Consider a triangular lattice in a 2D plane. The choice of a triangular lattice is for the convenience of rescaling of the system in the real space renormalization procedure. By enlarging the system by factor $\sqrt{3}$ and grouping every three sites into a "supersite", the number of the supersites is the same as the number of sites in the original system (see Fig.3). In Fig.3, the thin lines are for the original system and the thick lines are for the rescaled system. A supersite is regarded as empty if the majority of the three sites

are empty. Thus the concentration of the new system can be expressed as $p' = p^3 + 3p^2(1-p)$(Ref. [20]). Near the critical point $p_0 = 0.5$, on the metallic side, G can be written as $G = G_0(p-p_0)^t$, where the constant G_0 is proportional to the conductance of the unit cell. For the enlarged system this relation becomes $G' = G'_0(p'-p_0)^t$. In a 2D system the conductance is independent of the system size and we have $G = G'$. Thus, $t = \ln(\frac{G_0}{G'_0})/\ln(\frac{p'-p_0}{p-p_0})$. If the spin degree of freedom is frozen, the conductance of elementary cell is inversely proportional to the size of the cell, hence, $t = \ln(\sqrt{3})/\ln(\frac{3}{2}) = 1.35$. This value is very close to the exact value of $t = 4/3$ in the standard 2D percolation model. [21] When taking into account the spin degrees of freedom, as we discussed above, the p_0 point is also the critical point for the spontaneous magnetization. The conductance G_0 (or G'_0) is now associated with spin configurations. The spin dependence comes from the fact that G_0 is proportional to the average of conductivity between two nearest neighbor sites which is spin dependent,

$$\begin{aligned} G_0 &\sim \langle\sigma_{ij}\rangle \sim \left\langle \cos(\frac{\theta_i-\theta_j}{2}) \right\rangle \\ &= \frac{1}{A}\int_0^{\pi} d\theta_i \int_0^{2\pi} d\phi_i \int_0^{\pi} d\theta_j \int_0^{2\pi} d\phi_j \\ &\quad \times e^{-\beta m S\cos\theta_i} e^{-\beta m S\cos\theta_j} \cos(\frac{\theta_{ij}}{2}) \end{aligned} \tag{2.3}$$

The conductivity expression between nearest neighbor spin $\sigma_{ij} \sim \cos(\frac{\theta_{ij}}{2})$ comes from the double-exchange model where θ_{ij} is the angular difference between spins S_i and S_j ,which satisfies[22]

$$\cos\theta_{ij} = \cos\theta_i\cos\theta_j + \sin\theta_i\sin\theta_j\cos(\phi_i-\phi_j) \tag{2.4}$$

(θ_i, ϕ_i) denotes the orientation of spin S_i. A is a normalization constant. From the above equation, it is easy to show that $G_0 \sim m^2$. Because m can be written as $m \sim (p-p_0)$,[20] we finally get the conductance critical exponent in 2D triangular lattice as $t' \simeq 1.35 + 2 = 3.35$.

In the 3D case, we consider the normal cubic lattice. The elementary vectors of the enlarged lattice is just two times of those of the original one $\{\hat{e_x}', \hat{e_y}', \hat{e_z}'\} = \{2\hat{e_x}, 2\hat{e_y}, 2\hat{e_z}\}$. In this case $p' = \sum_{n=4}^{8} C_8^n p^n (1-p)^{8-n}$, from which we conclude that $p_0 = 0.395$ and $t = 1.7$ without spin effects. After the spin degrees of freedom are considered, the formula $G_0 \sim m^2$ is still satisfied. But in 3D case m has $m \sim (p - p_0)^{1.79}$.[20] So the critical exponent $t' \simeq 1.7 + 2 \times 1.79 \simeq 5.3$.

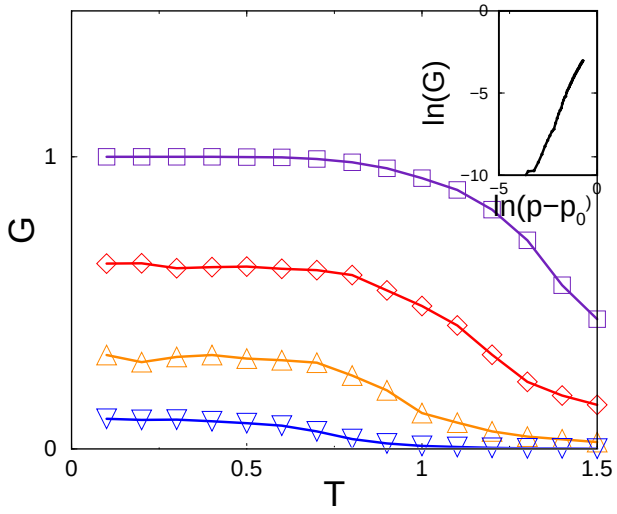

Figure 2.4. The normalized conductivity G as a function of temperature T in 2D model. From top to bottom, the concentrations are $p = 1.0, 0.9, 0.7, 0.6$ and 0.5. Inset: $logG$ vs. $log(p - p_0)$ shows a linear behavior with a slope $\simeq 3.5$

In Fig. 2.4 we show the numerical results of 2D conductance G. 3D calculation has not been done because of computational limit. The points with steepest drop are defined as the critical points for the metal-insulator transition. These points are consistent with the magnetic critical points (see Fig. 2.3), as we discussed before. In the inset of Fig.2.4 we show the $\ln(G)$ versus $\ln(p - p_0)$. They exhibit a linear dependence and the slope of the curve, corresponding to the exponent t, is roughly 3.5. This value is in a good agreement with the estimation from the renormalization group consideration although it is obtained from a different type of lattice structure.

In Table I we list the results of this work and compare them with the previous studies of the standard percolation theory[21] and experimental exponents in CMR materials.[10, 11] The experimental exponent t_3 (or t'_3) was obtained in the absence (or presence) of an external magnetic field.

TABLE 2.1. The critical exponent t for 2d and 3d cases. p_{c2} and p_{c3} are percolation threshold for 2d and 3d, respectively. t_d and t'_d are the critical exponents for d-dimension model without or with spin effects.

	p_{c2}	p_{c3}	t_2	t_3	t'_2	t'_3
exact numbers	0.5	0.31	1.33	1.9	-	-
experimental data	-	-	-	2.6	-	6.1
renormalization method	0.5	0.37	1.35	1.7	3.3	5.2
numerical results	0.51	0.32	1.30	-	3.5	-

Before summary, we would like to make couple comments. (i) In order to calculate the conductivity exponent, we have to determine the dependence of G_0 (see Eq.2.3) on the magnetization m, and the double-exchange model is used to achieve that goal. However, the double-exchange may not be the origin of the ferromagnetism in doped manganites, as shown in a recent work.[23] This might explain some of the discrepancy between the experimental and our theoretical values in the conductivity exponent. We should also mention that the values from the two experimental groups are not in good agreement with each other as seen in Table I. (ii) We have neglected the quantum effects in this work. This might be justified because T_c is relatively high in these samples. Develop a semi-classical transport theory in this problem is a difficult task because of the finite phase coherence length. There are attempts[24] of using the semi-classical theory to understand the two-dimensional metal-insulator transition.

2.5 Conclusion

In summary, we argue that the percolation threshold corresponds not only to the appearance of an infinite metal cluster, but also to the phase transition from PM to FM. This coincidence of two phase transitions renormalizes the critical exponents. The conductivity exponent has been obtained using real space renormalization and numerical calculations. The exponent is found to be quite different whether the magnetic transition is considered. This finding explains the large exponent discrepancy in some of the CMR materials in the presence or absence of an external magnetic field.

CHAPTER 3

Low temperature saturation of variable range hopping and delocalization of electron states by entanglement with phonons in two dimensions

ABSTRACT: We investigate low temperature transport properties in a two dimensional electronic system coupled with phonons. It is found that some of the localized states will be delocalized by the entanglement with phonons even when the temperature approaches the absolute zero. The distribution of phonons near the zero temperature is departed from the Boson distribution because the entangled states are preferred from the energy point of view. This leads to the low-temperature saturation of the variable range hopping of electrons and the existence of a metal-like behavior in two dimensions.

3.1 Introduction

The metal-insulator transition in two dimensional (2D) systems is of great interests in the last two decades. Within the standard scaling theory, all carriers are localized in the absence of an external magnetic field [25]. Seven years ago, metallic behavior was observed in Si-MOSFET [26]. Although the origin of this phenomenon is still in controversy, one school of thought believes that it is related to a crossover from the quantum to classical transport [27, 28, 29, 30, 31, 32]. Thus, the understanding of this phenomenon will shed light on the bridge connecting classical and quantum physics and may introduce new concept on the transport in low dimensions. One mechanism leading to the transition from quantum to classical behavior is the inelastic scattering of electrons by phonons or other bosonic excitations which eliminates the quantum coherence of electron wavefunctions. In early years the phonon-assisted transport of electrons has been studied by many authors. In his pioneering work Mott has proposed variable range hopping (VRH) model describing finite conductance of amorphous semiconductors at finite temperatures [33]. In this model the hoppings between quantum-mechanically localized states are assisted by phonons. Other authors have theoretical studied the delocalization effect of phonons in disordered systems [34, 35, 36, 37]. This effect, however, has been shown to vanish at the zero temperature due to the usage of the Bose thermal distribution for free phonons in these studies. It is believed that at zero temperature the metal-insulator transition is still related to a quantum transition, and the 2D systems should have zero conductance in this sense. In VRH model the classical-like processes connected with inelastic scattering vanish when approaching to zero temperature, leading the the $T^{-\frac{1}{3}}$ divergence of the logarithmic resistance in 2D. Recently, the vanishing of classical-like behavior at zero temperature is questioned experimentally by the observations of the low-temperature saturation of the dephasing [38]. A theoretical calculation on quantum dot has shown that the inelastic scattering for the electron can not vanish

at zero temperature, leading to the saturation of the dephasing. This implies that the combined electron-phonon states, rather than the separated ones, are in equilibrium with the thermal bath [39]. A 2D electronic system coupled with phonons is studied here. We focus on the delocalization effect of phonons at the zero temperature. According to the Heisenberg uncertainty principle, the entanglement of electron and phonon states lowers the energy of the combined system. From this the VRH theory is extended to the case of temperature approaching to the absolute zero by replacing the Bose distribution for free phonons with the thermal statistics of the coupled electron-phonon system. We argue that such kind of phonon-assisted mechanism can also saturate at very low temperatures, leading to the metal-like behavior.

3.2 Coupled electrons and phonons

At the beginning let us consider a model Hamiltonian that describes the coupling between electrons and phonons in a 2D disordered system

$$H = \sum_i \epsilon_i c_i^\dagger c_i + \sum_{\langle i,j \rangle} (c_i^\dagger c_j + \text{H.c.}) + \sum_{i,q} g_{i,q} c_i^\dagger c_i (a_q^\dagger + a_q) + \sum_q \hbar\omega_q \left(a_q^\dagger a_q + \frac{1}{2} \right), \quad (3.1)$$

where c_i and $c_i^\dagger$ are electronic annihilated and creation operators for electrons at site i, ϵ_i is the random site energy uniformly distributed between $-w/2$ and $w/2$, $a_q^\dagger$ and a_q are annihilated and creation operators for phonons of mode q, $\hbar\omega_q$ is energy of a phonon in mode q, and $g_{i,q}$ is the coupling strength between electron at site i and phonon of mode q which is randomly distributed between 0 and q. Here the second term describes the nearest-neighbor hopping of the electrons and the hopping integral is set to be the energy units. We assume that only a fraction of the phonon modes has enough coupling strength with electrons, and the number of these modes M is proportional to the area of the system, $M = \alpha N^2$, with α being a constant and N the linear size of the system.

We restrict ourselves to the study of the electron-phonon coupling and the correlation between electrons is ignored, thus, we only consider the motion of one

electron on a lattice. A full quantum-mechanical description of a state in Hamiltonian (1) is a linear combination of basis wave functions consisting of an electron state and a number of phonons:

$$|\Psi\rangle = \sum_{i,\mathcal{D}} C_{i,\mathcal{D}} |\phi_i\rangle \bigotimes \prod_{q\in\mathcal{D}} a_q^\dagger |0\rangle, \tag{3.2}$$

where $|\ \phi_i\rangle$ is the electron orbital on site i, $\mathcal{D}$ is a set of phonon numbers with m_q being the number in the qth mode for q ranging from 1 to M, $|\ 0\rangle$ is the state with zero phonon, and $C_{i,\mathcal{D}}$ is the corresponding coefficient. It is interesting to note that by this description the Hilbert space for the motion of a single electron is extended from $N\times N$ dimensions in the case without the electron-phonon interaction to $N\times N\times(m+1)^{\alpha N\times N}$ dimensions, if we only include at most m phonons for each mode ($m_q \leq m$ for all sets $\mathcal{D}$). This is a tremendous increase of the effective dimensions of the system even though $g_{i,q}$, α and m is small, and may lead to the violation of the conclusion of the scaling theory in Ref. [25]. The Hilbert space consists of a large number of planes, each of which corresponds to a specific set of the phonon states. Among them the basic plane is the one with zero phonon, in which the site energies are the original values given by ϵ_i in Hamiltonian (1). For the other planes the site energies are increased by an amount of the energies of the corresponding phonons. This increase of site energies may weaken the effect of tunneling paths provided by these planes. However, this effect still can not be neglected if there is a small fraction of phonon modes which has low energies and is strongly coupled with electrons.

3.3 Transfer matrix method

To illustrate this effect we use the standard transfer matrix method (TMM) to study the delocalization of the electronic states on a 2D disordered system via the coupling with phonons. To simplify the calculation, we only include at most one phonon for each mode, and the phonon induced hoppings between different sites are ignored. We calculate the rescaled localization length, λ_N/N, where λ_N is the

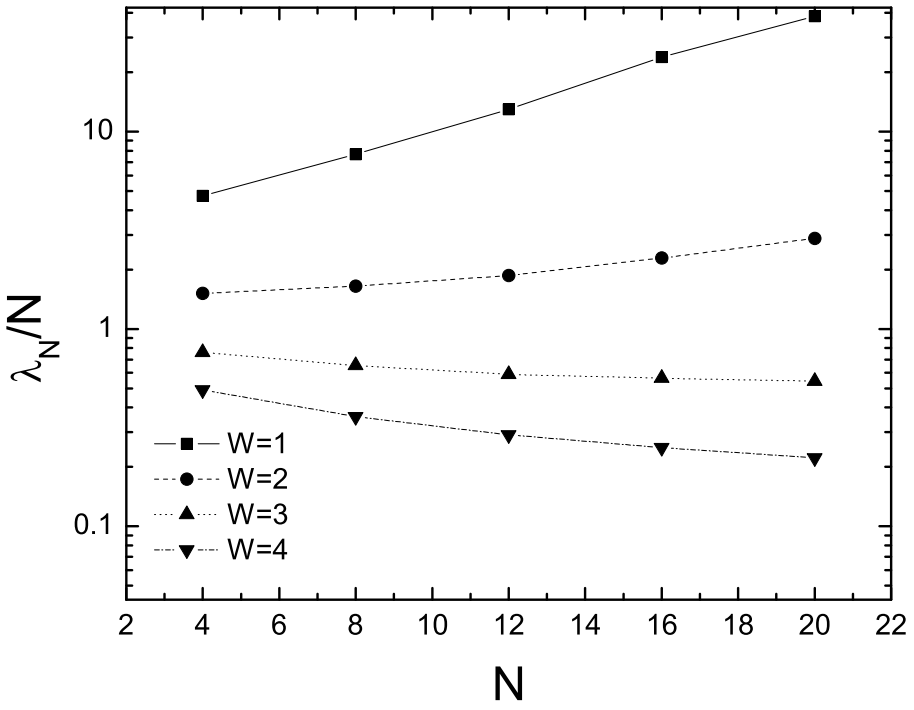

Figure 3.1. Rescaled localization length as a function of the system size. The parameters are: $g = 0.2$, the energy of electron is 0.1, the density of relevant phonon modes is described by $\alpha = 1/16$, and the phonon energy is $\hbar\omega = 0.2$.

localization length of a strip with width N and length L, much larger than N. The number of phonon modes involved in this calculation is αN^2, corresponding to the number of modes in a $N \times N$ square. Thus, the obtained rescaled localization length corresponds to the conductance of the square system. In the TMM calculation we project the input and output amplitudes of the wave function to the basic plane with zero phonon, although there are many planes with non-zero phonons in the intermediate states. This procedure guarantees the incoming and outgoing electrons is from and to the zero-temperature reservoirs. In Fig. 3.1 we plot the size dependence of the rescaled localization length for different strengths of disorder W. It is obvious that there appear states for which the rescaled localization length is increased with the system size. This behavior could be regarded as metallic-like. However, with this calculation we could not determine a sharp point of the transition, as there is not a value of W_c, for which the rescaled localization length is size independent (fixed point). This implies the failure of the use of the standard TMM, since the increase of the effective dimensions with the size N is rather non-regular, and the processes involved are in fact not quantum mechanical. Nevertheless, the trend of the delocalization is evidently shown from this calculation. This trend occurs at the zero temperature. The tunneling paths in planes corresponding to non-zero phonons can be considered as "virtual processes", which have effect even at the zero temperature. Especially, if $\hbar\omega \ll W$, the paths with non-zero phonons can always provide tunneling probability for the originally localized states.

3.4 Variable range hopping model

A more suitable description for these processes is some type of the classical treatments, such as the VRH model or the percolation theory. However, as mentioned above, in the previous VRH model the effect of phonons vanishes at the zero temperature. This is because the number of phonons is zero if the phonon system is

regarded as in equilibrium with the thermal bath. This is true only if the energy of the total system of electron and phonons is exactly equal to the sum of the electron energy and the phonon energy. In this case the statistical distribution function is the product of those of the subsystems [40]. The situation will be changed when the coupling between the subsystems alters the energy of the total system from the sum of the subsystems. In this case the energies of the subsystems are no longer a meaningful quantities which can be used in the ensemble averaging. The only quantity which can be used is the total energy. In a simplest situation let us consider an electron at a single energy level coupled with a phonon mode of energy $\hbar\omega$ and the coupling strength is g. If the energy change is considered as far as to the second order of g, the phonon number at temperature T is

$$p(\omega, T) = \frac{\frac{\exp(-\beta\hbar\omega)}{((1-\exp(-\beta\hbar\omega))^2} + \frac{g^2}{\hbar^2\omega^2}\exp(\beta g^2/\hbar\omega)}{\exp(\beta g^2/\hbar\omega) - 1 + \frac{1}{1-\exp(-\beta\hbar\omega)}}. \tag{3.3}$$

Here, $\beta = \frac{1}{kT}$ with k being the Boltzmann constant. It can be seen that the phonon number saturates to $\frac{g^2}{\hbar^2\omega^2}$ at low temperature which is different from the usual Bose distribution. On the other hand, for $kT \gg \frac{g^2}{\hbar\omega}$, the thermal fluctuations smear out the energy difference caused by the coupling, the phonon number becomes the same as that of the phonon subsystem. Of course, in a real world there are many phonon modes coupled to many electron states, and the combined states become more entangled and complicated.

In Fig. 3.2, we compare the above equation with numerical results by diagonalizing the Hamiltonian. The electron subsystem is a 10×10 square lattice with on-site disorder and nearest neighboring hopping. The maximum number of phonons in the state $\hbar\omega$ is considered up to M, $M = 16, 32$. This will limit the statistically averaged phonon number p, leading to a finite value of p in the numerical results even at the limit of $\omega = 0$ which corresponds to a complete softening of the lattice. During the calculations, it is found that the strength of the on-site disorder in the electron plane has little effect on the average phonon number. So we take $w = 0$ as default

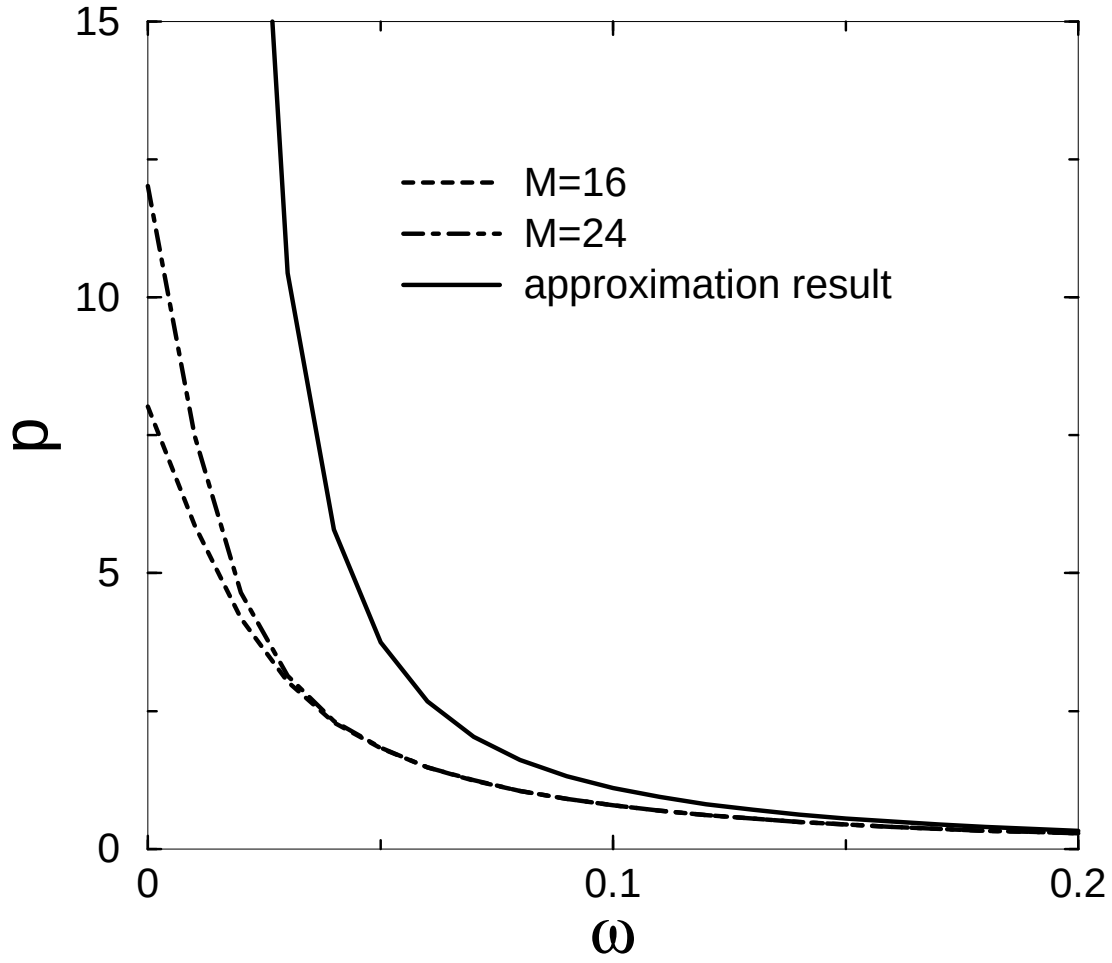

Figure 3.2. The distribution of phonons p as a function of ω. The parameters are: $w = 0$, $g = 0.1$ and $kT = 0.1$.

in all calculations. It seems that the result from the approximation in Eq. (3.3) tend to overestimate the phonon number compared with the numerical results when ω is small. However, it does indicate the basic fact that the coupling with the electron system will excite more phonons than that from the ordinary Bose statistics for an isolated phonon system in equilibrium with the bath and, especially, the average phonon number saturates to a finite value in approaching to the zero temperature. So, for simplicity we will use this approximate result in the next stage.

In the VRH model the electron can be transferred from one localized state to another localized state with the assistance of phonons. This can produce a finite conductance even though all the states of electrons are localized. According to Mott, the VRH process takes place in a lattice with the following Hamiltonian:

$$H_{\mathrm{VRH}} = \sum_m \xi_m n_m, \tag{3.4}$$

where index m denotes a localized state, ξ_m is the corresponding energy, and $n_m = 0, 1$ is the occupation of electrons in this state. The probability of transferring of an electron from a localized state m to another localized state m' $P_{mm'}$ is obviously proportional to the number of the available phonons, but exponentially decays with the distance between the localization centers of states m and m' denoted as $r_{mm'}$. This consideration leads to the following expression [33]:

$$P_{mm'} \propto \exp\left(-\frac{2r_{mm'}}{\lambda}\right) p(E_{mm'}, T), \tag{3.5}$$

where λ is the average localization length of the electron states and $E_{mm'}$ is the energy difference between states m and m', assumed to be the same as the energy of the mediated phonon. In the Mott theory $P_{mm'}$ vanishes at zero temperature since from the ordinary Bose distribution the number of phonons is zero. However, this probability should be finite at zero temperature if we calculate it from the pure quantum mechanics of the electron system, since the electron-phonon coupling produces non-diagonal elements for states $\{m\}$. A straightforward perturbation estimation from the coupling in Hamiltonian (1) gives $P_{mm'} \propto \frac{g^2}{(\hbar^2\omega + E_{mm'})^2} \exp\left(-\frac{2r_{mm'}}{\lambda}\right)$. This coincides with

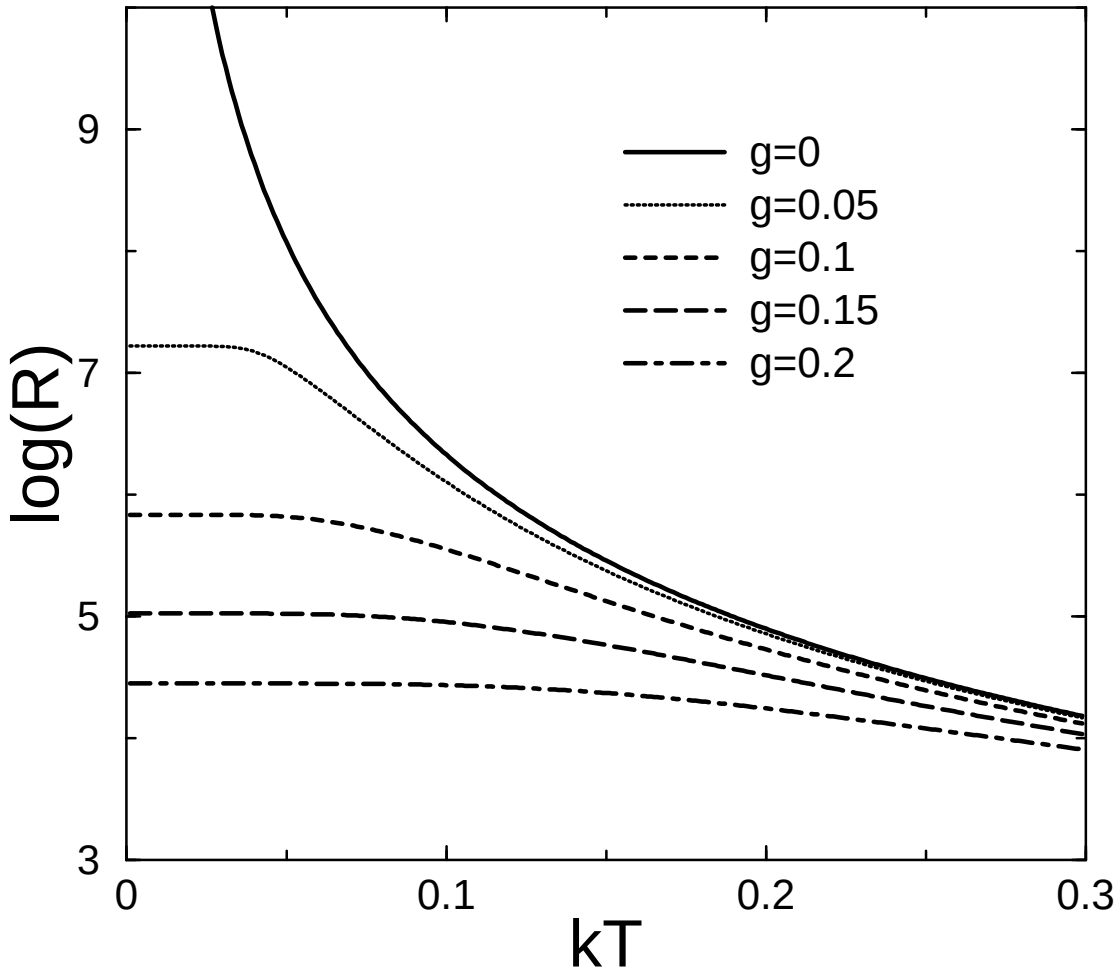

Figure 3.3. Resistivity as a function of the temperature. The parameters are: $\lambda = 1$ and $\rho = 0.6$.

Eq. (3.5) at $T \to 0$ if $p(E_{mm'}, T)$ is replaced with Eq. (3.3). Thus, it is reasonable to replace the Bose distribution with the phonon number in the composite electron-phonon states so that the VRH theory can be generalized to the low-temperature and strong electron-phonon coupling limit.

The resistivity of the system is proportional to the inverse of the maximum probability with respect to the variation of $r_{mm'}$, and the energy difference $E_{mm'}$ is approximated by

$$E_{mm'} = \frac{1}{\rho r_{mm'}^2}, \tag{3.6}$$

where ρ is a quantity proportional to the density of states of electrons. In Fig. 3.4 we plot the temperature dependence of the resistivity obtained from the above consideration. It can be seen that there exists states with finite resistivity at zero temperature. For this states the resistivity is almost saturated at low temperatures. If the scattering effects of the thermal excitations are included, the metallic-like behavior of the temperature dependence could be expected in this regime. On the other hand, the transition probabilities between localized states are randomly distributed. Among them the states with transition probabilities larger than a certain threshold can be connected to form clusters that are similar to those in classical percolation models. In this sense the percolation models may also be suitable for the description of the metal-insulator transition in such systems.

In summary, we have investigated the effect of the electron-phonon coupling on the transport of electrons in 2D disordered systems at very low temperatures. The delocalization effect of phonons, which has been studied in the case of finite temperatures in earlier works [33, 34, 35, 36, 37], is investigated in the case of temperature approaching to the absolute zero. Due to the redistribution of the phonon number in the composite states of electron and phonons, the VRH theory is modified at the low-temperature limit, and the saturation of the VRH probabilities can produce a finite value of the resistivity at the zero temperature and the metallic-like behavior of the

system, which can not be accounted for by the theory of the quantum metal-insulator transition.

CHAPTER 4

Spin Entanglement and “0.7 Anomaly” in Quantum Point Contact

ABSTRACT: Spin entanglement between itinerant and localized electrons in a short one-dimensional chain with low Fermi energy and its effect on transport properties are investigated. As long as the entanglement between itinerant and localized electrons is maintained, a 3/4 quantum conductance occurs due to the blockade for the singlet state but no effect on the triplets. This will result in an observation of conductance near \0.7". We find that this blockade effect is complete as the effective coupling between itinerate and localized electrons exceeding a threshold. The many-body correlation of electrons near the band edge reduces this accessibility at low temperature and causes specific temperature dependence of the conductance. These results provide a natural explanation for the “0.7 anomaly” in quantum point contacts.

4.1 Introduction

Entanglement of indistinguishable particles is one of the most amazing concepts introduced by quantum mechanics. Represented naturally in a many-body Hilbert space, the wavefunction of an entangled state will introduce simultaneous quantum coherence among particles, which will dramatically change the behaviors of a quantum system, such as transmission.

The quantization of the conductance in mesoscopic systems has been observed in quantum point contacts (QPC) where a series of plateaus at multiples of $2e^2/h$ appears in curves of conductance G versus gate voltage V_g [41, 42]. Prior to the first integer plateau, a shoulder of $0.7(2e^2/h)$ has often been observed and is called the "0.7 anomaly" [43, 44, 45, 46, 47]. In Ref. [47] it is suggested that the anomaly originates from the 3:1 triplet-singlet statistical weight ratio if itinerate electron and localized electron form an entanglement state.

In this chapter, we investigate the effect of spin entanglement between itinerant and localized electrons on the transport through a one-dimensional (1D) system with low electron density or Fermi energy. We show that this entanglement leads to a $\frac{3}{4}$, rather than an integer, quantization of the conductance due to the full blockade of the singlet entangled channel. Different from that in high Fermi energy case, a renormalization-group (RG) calculation reveals an inverse temperature dependence against that of the well known Kondo effect[48]. More RG results will be discussed in the next chapter. Our theoretical results are in qualitative agreement with experimental data in quantum point contacts (QPC). The effect of dephasing in longer systems is also discussed. We show that this entanglement, together with the correlation effect of electrons near the band edge, is the basic physics behind the "0.7 anomaly" observed in QPC.

Since relevant states undergo empty, single and double occupations even within the width of one plateau or shoulder, including global charge variations and fluctuations in calculations is important. The "0.7 anomaly" appears only prior to the first integer plateau, and only at relatively higher temperatures, for which the intensity of the Kondo effect is negligible. The shape of the shoulder is much different from the two resonance peaks of the singlet and triplet states [50], and there is no evidence of the attractive interaction from which two-electron bound states can be formed [47]. To address the above mentioned questions, in this chapter we theoretically study the transport through a quantum point contact(QPC) by using a model which includes the Coulomb interaction, the charge fluctuations, and the multi-channel structure on an equal footing. By using the singlet-triplet representation to label spin states of the tunneling electron and the local electron, we show a wide anti-resonance for the singlet channel near the band bottom, giving rise to the 0.75 shoulder. The shoulder is complemented to 1 by the formation of a Kondo singlet at low temperatures, and manifests itself at higher temperatures when the Kondo singlet collapses. Thus, the role of the Kondo singlet is to suppress the anti-resonance, quite different from the Kondo physics discussed in Ref. [48]. A simple scaling curve for conductance is obtained and is found to compare well with the experimental one. The results provide consistent explanations for a wide range of characteristics observed in experiments.

A QPC can be described with a narrow and short bar connected to the left and right leads which serve as reservoirs. Thus, one obtains several continuous 1D subbands. Some local states, may be virtual bound states[48], can be created by the specific QPC geometry. These states are isolated from the leads and should not be included in the band continuum. The potential of the bar area, including both the band continuum and the local states, is tuned by the gate voltage. The single-electron energies of subbands and levels are shown in Fig. 4.1(a). We include on-site Coulomb repulsion U of electrons confined in each local states. In equilibrium the Fermi energy of reservoirs is fixed and we set it as energy zero. The occupations of

state are controlled by tuning the gate voltage. In Figs. 4.1(b), 4.1(c) and 4.1(d) we show the empty, single and double occupations of the local state most adjacent to the band bottom. When the Fermi level crosses the band bottom, the first subband contribution to the conductance causes the first plateau to appear. At this moment most of the local states are fully occupied and have no effect on the transport, except the one closest to the band bottom which may be singly occupied due to the on-site interaction. It is sufficient to only include this state in our model. By tuning V_g further this local state is also fully occupied and the plateau structure is determined only by the subbands.

4.2 Many body effect on transport

The Hamiltonian of the system can be written as

$$\begin{aligned} H = & \sum_{m,i,\sigma} t_0 (a^\dagger_{m,i,\sigma} a_{m,i+1,\sigma} + \text{H.c.}) \\ & + \sum_{m,i,\sigma} [(m-1)\delta_0 - eV_g] a^\dagger_{m,i,\sigma} a_{m,i,\sigma} \\ & + \sum_{\sigma} t' (a^\dagger_{1,0,\sigma} d_\sigma + \text{H.c.}) + \sum_{\sigma} (\epsilon_0 - eV_g) d^\dagger_\sigma d_\sigma \\ & + U d^\dagger_\uparrow d_\uparrow d^\dagger_\downarrow d_\downarrow, \end{aligned} \tag{4.1}$$

where $a_{m,i,\sigma}$ and d_σ are the annihilation operators of electrons on the ith site of the mth continuum channel and at the local state, respectively, with σ being the spin index. δ_0 is the energy spacing between subband bottoms. ϵ_0 stands for the position of the local state. $t_0 = 1$ is the hopping integral of the channels, and t' is the coupling of the lowest channel and the bound state at a site ($i = 0$). Only the coupling of the local level to the lowest channel ($m = 1$) is considered, because local level coupling has no effect on the transmission in higher channels due to the double occupation.

For $V_g \ll 0$ and at the zero temperature, the potential is too high and the states in the bar, including the local state and the continuum chains, are empty.

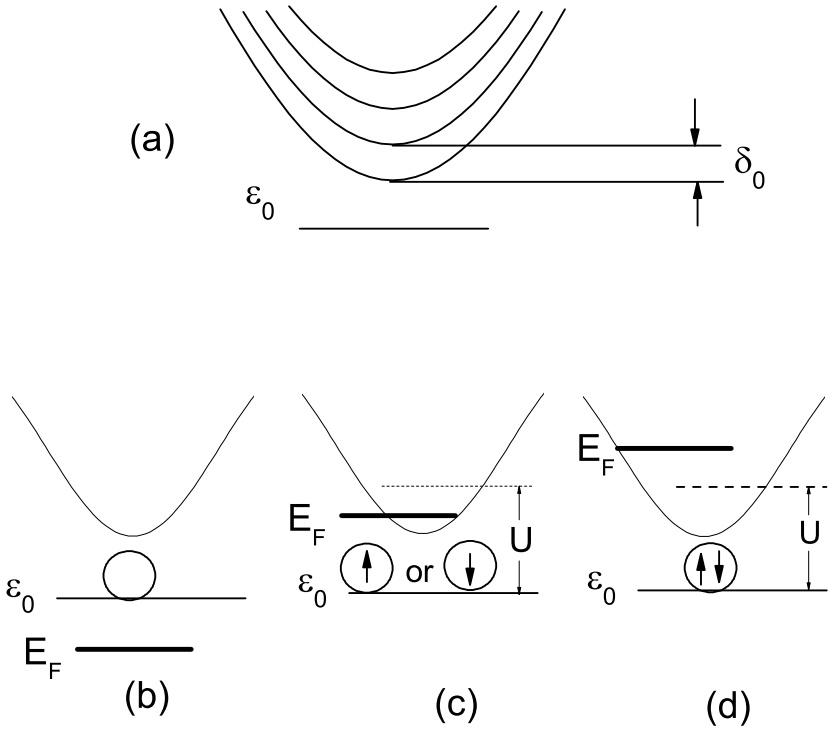

Figure 4.1. (a) Sketchy illustration of dispersion relation of 1D subbands and local states. δ_0 is energy spacing between subbands, and ϵ_0 is the position of the local state. (b) Empty state. E_F denotes the Fermi level. (c) Singly occupied state. (d) Doubly occupied state.

With V_g increasing , the local state becomes singly occupied as $\epsilon_0 < eV_g < \epsilon_0 + U$. when $eV_g > \epsilon_0 + U$, the local state is doubly occupied and has no effect on the conductance. On the other hand, the mth continuum channel gives $2e^2/h$ contribution to the conductance if $eV_g > (m-1)\delta_0 - 2t_0$, because in this case the Fermi level is higher than the bottom of this subband. This provides the integer plateaus in the G-V_g curves with plateau width δ_0/e.

Since the local level is below the bottom of the whole band continuum, the tunneling in the first channel is affected by its charge and spin states. There are 4 states of the local level: the empty, $|\phi_1\rangle = |0\rangle$, the spin up and down single occupation, $|\phi_2\rangle = |\uparrow\rangle$ and $|\phi_3\rangle = |\downarrow\rangle$, and the double occupation, $|\phi_4\rangle = |\uparrow\downarrow\rangle$. If an electron is injected into the channel, it will be scattered by the state on the local level. At first we consider only the tunneling and local electrons and ignore the other electrons in the Fermi sea. These considered electrons form a many-body state

$$|\psi\rangle = \sum_{n=1}^{4} \sum_{i,\sigma} p_{n;1,i,\sigma} |\phi_n\rangle \bigotimes |1,i,\sigma\rangle, \tag{4.2}$$

where $|1,i,\sigma\rangle$ is the orbital at site i with spin σ in the first channel, and $p_{n;1,i,\sigma}$ is the corresponding coefficient. By applying the Hamiltonian on $|\psi\rangle$ one obtains the Schrödinger equations for the coefficients. These equations can be expressed with an equivalent single-particle network in which every site represents a combination of indices $(n;1,i,\sigma)$ of the coefficients [51]. In the present case the network is an 8-channel one where every channel stands for a combination of n and σ, and a site in a channel corresponds to a coordinate i in the chain. In the network the channels with $(n=2,\sigma=\uparrow)$ and $(n=3,\sigma=\downarrow)$, and the channels with $n=1,4$, corresponding to the empty and doubly occupied local states, are independent. The other 2 channels are connected at site $i=0$ but can be easily decoupled with the transformation $|S,i\rangle = \frac{1}{\sqrt{2}}(|\phi_2\rangle \bigotimes |1,i,\downarrow\rangle - |\phi_3\rangle \bigotimes |1,i,\uparrow\rangle)$ and $|T,i\rangle = \frac{1}{\sqrt{2}}(|\phi_2\rangle \bigotimes |1,i,\downarrow\rangle + |\phi_3\rangle \bigotimes |1,i,\uparrow\rangle)$. The final network with 8 independent channels is shown in Fig. 4.2. For single occupation there is one singlet channel with one scatterer (6) and three pure triplet

channels (3, 4, and 5) without scattering by the local level. Different from Ref. [47], the singlet-triplet notation used here is merely to label spin states of the tunneling and local electrons that are not bound together. For $m > 1$ and for the non-scattering pure channels of $m = 1$, the transmission coefficient is

$$\tau_m(\epsilon) = \begin{cases} 1, \text{ for } |\epsilon - (m-1)\delta_0 + eV_g| < 2t_0, \\ 0 \text{ otherwise.} \end{cases}, \tag{4.3}$$

where ϵ is energy of the injected electron. For the singlet (empty) channel of $m = 1$ with scattering center,we can write down the effective Hamiltonian of these channels:

$$H = \sum_{i=-\infty}^{\infty} (c_i^\dagger c_{i+1} + c_{i+1}^\dagger c_i) + t'(c_0^\dagger d + d^\dagger c_0) + \epsilon_d d^\dagger d \tag{4.4}$$

, where the first term represents the kinetic motion of electron in the first subband, the second term is the hopping term from the first subband to the scattering center d. ϵ_d is the energy of the scattering center. $\epsilon_d = \epsilon_0$ for the empty channels and $\epsilon_d = \epsilon_0 + U$ for the singlet channel.

The transport properties can be solved exactly by injecting a electron whose state is plane wave with wavevector k

$$\Phi(x) = \begin{cases} \mathrm{e}^{ikx} + re^{-ikx} & \mathrm{x} \leq -1 \\ \mathrm{te}^{ikx} & \mathrm{x} \geq 1 \\ \Psi_0 & \mathrm{x{=}0} \\ \Psi_1 & \mathrm{x{=}d} \end{cases} \tag{4.5}$$

where r and t are the reflection rate and transmission rate, respectively. Ψ_0 is the state at the center and Ψ_1 is the state at the scattering center. The transmission

coefficient is $\tau = |t|^2$. r, t, Ψ_0 and Ψ_1 are derived from this equations,

$$\begin{aligned} H\Phi(x) = E\Phi(x) &\longrightarrow \\ E(e^{-ik} + re^{ik}) &= e^{-2ik} + re^{2ik} + \Psi_0 \\ E(te^{ik}) &= te^{2ik} + \Psi_0 \\ E(\Psi_0) &= e^{-ik} + re^{ik} + te^{ik} + t'\Psi_1 \\ E(\Psi_1) &= \epsilon_d\Psi_1 + t'\Psi_0 \end{aligned} \tag{4.6}$$

where $E = 2\cos(k)$.

$$\tau_{\mathrm{s(e)}} = \frac{4[u_{\mathrm{s(e)}} - 2\cos(k)]^2 \sin^2(k)}{v_{\mathrm{s(e)}}^4 + 4[u_{\mathrm{s(e)}} - 2\cos(k)]^2 \sin^2(k)} \tag{4.7}$$

for $|\epsilon + eV_g| < 2t_0$ and $\tau_{\mathrm{s(e)}} = 0$ otherwise, where k is the momentum of the tunneling electron determined by $\epsilon = 2t_0\cos(k) - eV_g$, and $u_{\mathrm{s}} = (\epsilon_0 + U)/t_0$, $u_{\mathrm{e}} = \epsilon_0/t_0$, $v_{\mathrm{s}} = \sqrt{2}t'/t_0$, $v_{\mathrm{e}} = t'/t_0$.

4.3 Results

For the singlet channel the scatterer produces an anti-resonance at $\epsilon = \epsilon_0 - eV_g + U$ with a zero transmission coefficient at the minimum and with semi-width $t'^2/t_0|\sin(k)|$. Near the subband bottom where we focus, $\sin(k) \sim 0$, so the width of the transmission dip is extremely large even though t' may be much smaller than t_0. As a result, the dip of τ_s develops to a flat plateau with nearly zero height. This is different from the results of Ref. [50] where the singlet and triplet states give two separate resonance peaks with different weights. Without the magnetic field and ignoring the effects of other electrons, in the range of single occupation the conductance is governed by $e^2/2h$ times the sum of the transmission coefficients of the singlet and triplet channels which are non-zero only for the tunneling electron with energy higher than the subband bottom. Here the prefactor 1/2 stands for the weight of one spin state of the local electron. As mentioned above, $\epsilon_0 \lesssim -2t_0$, so $\epsilon_0 + U$ may be above the subband bottom. Thus, in the range of $-2t_0 < eV_g < \epsilon_0 + U$ conductance plateaus at height $0.75(2e^2/h)$. For $eV_g > \epsilon_0 + U$, the conductance is dominated by the double-occupation channels (7 and 8 in Fig. 4.2), leading to a jump from 0.75 to 1 at $eV_g = \epsilon_0 + U$. This is the origin of the 0.7 anomaly within our model.

When the local spin and conduction electrons form a many-body state, the accessibility of the local state by an electron tunneling from one lead to the other will be changed. This effect changes the effective hopping $\bar{t}'_{0,0}$ and can be calculated from the spectral density (SD) of the Green function (will be discussed in the next chapter) defined as $G_\sigma = \langle\langle d_\sigma d_\sigma^\dagger \rangle\rangle$. At temperature T_n associated with the nth RG step, one has

$$\bar{t}'^2_{0,0}(T_n) = t'^2_{0,0}\rho(T_n), \tag{4.8}$$

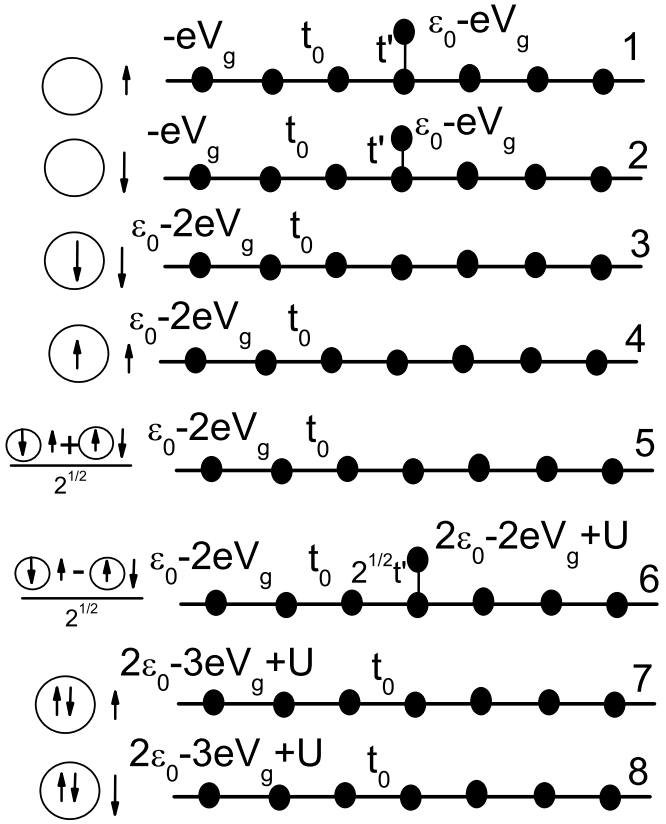

Figure 4.2. Eight independent channels for a tunneling electron. The state of the local level is illustrated by circles, and the spin of the tunneling electron is represented by an arrow outside the circle.

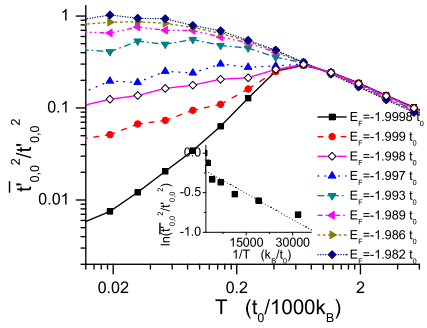

Figure 4.3. $\bar{t'}^2_{0,0}/t'^2_{0,0}$ as a function of T. The energy of the local state is below the Fermi level by $10^{-3}t_0$ and the Coulomb repulsion U is $2\times10^{-3}t_0$. The hopping integral $t' = 0.02t_0$. The insert shows $\ln(\bar{t'}^2_{0,0}/t'^2_{0,0})$ as a function of $1/T$ for the case of $E_F = -1.998t_0$. The dotted line is a fitting function $\ln(\bar{t'}^2_{0,0}/t'^2_{0,0}) = \ln a - T_A/T$ with $k_BT_A = 0.000044t_0$.

where $\bar{\rho}(T_n)$ is the SD averaged in an energy window determined by $\left(-\frac{\partial f(\epsilon,T_n)}{\partial\epsilon}\right)$ at $\epsilon = E_F$. The SD can be calculated as

$$\rho(\omega,T_n) = \frac{1}{Z_n}\sum_{p,p'}|d^{n,\sigma}_{p,p'}|^2\delta(\omega - E^n_{p'} + E^n_p)$$

$$\times\left[\exp\left(-\frac{E^n_p}{k_BT_n}\right) + \exp\left(-\frac{E^n_{p'}}{k_BT_n}\right)\right], \tag{4.9}$$

where Z_n is the partition function, $d^{n,\sigma}_{p,p'}$ are the matrix elements of operator d_σ in the representation of eigen-wavefunctions, and E^n_p is the pth eigen-energy at the nth RG step. The values of $d^{n\sigma}_{p,p'}$ can be evaluated recursively in the iteration [58].

In Fig. 4.3, we plot $\bar{t'}^2_{0,0}/t'^2_{0,0}$ verse T for different values of the Fermi level. The curves reflect the behavior of the SD near the Fermi level. For higher Fermi level the SD exhibits the usual $1-\alpha T^2$ behavior of the ordinary Kondo effect. By lowering the Fermi level, the SD begins to decrease with decreasing temperature, resulting in a peak. In the RG calculation the contributions to the SD are from the layers of the onion with statistical weights exponentially decaying from the outer to the inner. The states in the outer layers are more extended, the kinetic energy will be enhanced

if an electron is transferred from these layers to the local impurity. This prohibits the access of these layers to the impurity in the case of low Fermi level. In decreasing the temperature, the number of onion layers increases. For low Fermi level, the outer layers newly added cease to contribute to the SD after a temperature, as the electrons in these layers can not access the impurity state. Thus, the SD will begin to decrease as the statistical weights of the inner layers $e^{-T_A/(2T)}$, where T_A corresponds to a characteristic energy associated with the many-body correlation.

This abnormal temperature dependence of SD can also be understood in a more physical way. As the Kondo effect emerging, the conduction electrons tend to localize around impurity state forming the Kondo cloud to screen the impurity. But as the Fermi surface is near the band bottom, the extensive nature of the states at the Fermi surface will prohibit the formation of the Kondo cloud.

For low E_F the conductance is $G(T) \approx \frac{2e^2}{h}\left(1 - \frac{a^2 e^{-T_A/T}}{2t_0\Delta^3}\right)$. For higher temperatures we have $\bar{t'}_{0,0} > t'_{\text{thre}}$ and $G(T) \approx 0.75\frac{2e^2}{h}$, and for lower temperatures $\bar{t'}_{0,0} < t'_{\text{thre}}$ and $G(T) \approx \frac{2e^2}{h}$. Thus, we reproduce the transition from full quantization of the conductance to $\frac{3}{4}$ quantization. The temperature dependence of the conductance in this transition is in agreement with the experiments of QPC [53]. In fact, if a Kondo cloud was formed, its size would be $\hbar v_F/k_B T_K$, with v_F being the Fermi velocity that approaching zero in the present case. This would enhance the energy of the Kondo cloud due to the size effect. Thus, at very low temperatures the Kondo cloud collapses and the accessibility of the singlet channel to the local state is reduced.

As the quantum point contact becomes longer and longer, the entanglement for charge may be destructed but not for spin entanglement. Because the spin coherent length is usually much longer than charge coherent length. So at this moment, among the one-occupied 4 channels we discussed above, 3rd and 4th channels are still good quantum state because the spin of conduction and local electrons are pointing to the same direction. But this is not for the 5th and 6th channels. With dephasing, the 2 new good quantum channels will be the linear combination of 5th and 6th channels.

The scattering will be introduced to these channels by the 6th channels. So in this case, total two channels will be blocked by the antiresonance but not one, resulting $0.5\frac{2e^2}{h}$ conductance shoulder. This is in good agreement with the experimental observation.

4.4 Conclusion

At low temperatures P_l and $f(\epsilon)$ can be approximated with step functions and for $-2t_0 < eV_g < \epsilon_0 + U$, the conductance becomes

$$G(T) = \frac{2e^2}{h}\left(\frac{3}{4} + \frac{1}{4}F(\widetilde{T})\right), \tag{4.10}$$

where $F(\widetilde{T})$ is a universal function of rescaled temperature $\widetilde{T} = T/T_K$, describing the influence of the Kondo effect. Here, the range of F is $[0, 1]$, the prefactor of F is $1/4$ and the constant is $3/4$, reflecting the fact that the formation of the Kondo singlet influences only the contribution from the singlet channel. In Ref. [54], the same functional form is used for $G(T)$, however, the corresponding prefactor and constant are both $1/2$. But the range in which the measured points can be fitted well by a universal function is only from $1/2$ to 1, as can be seen from Fig. 2(b) in Ref. [54]. This implies that the experimental data only confirm the $1/4$ of the conductance that is influenced by the Kondo effect. The other $1/4$ may also vary with temperature but perhaps due to other physical influences. In Ref. [55], from the data of quantum dots the prefactor is 1 and the constant is 0, implying the full Kondo effect for the tunneling. This may indicate the consequence of different structures between a QPC and a quantum dot: the Kondo impurity is an extra local level in QPC as studied in this work while it may be embedded in the tunneling path in quantum dots. It is known that there is no anti-resonance associated with the latter case [56]. It is easy to see that at low T $F(\widetilde{T}) \sim 1 - p_k(T) = 1 - tanh(-T/T_K)^2$.

By applying a bias voltage V_b between two leads the current is $I = \frac{2e}{h}\int d\epsilon[f(\epsilon - eV_b/2) - f(\epsilon + eV_b/2)]\tau(\epsilon)$, function $F(\widetilde{T})$ in Eq.(4.10) becomes $F(\widetilde{T})\exp[-(eV_b/w)^2]$,

reflecting the width w ($\sim k_B T_K$) of the Kondo peak in the spectral density [57]. We calculate the differential conductance $g = \frac{dI}{dV_b}$, shown in the upper inset of Fig. 3. The zero-bias peak, originated from the Fermi-level dependence of the Kondo effect, exists only at low temperatures for which the 0.7 shoulder is complemented to 1. By applying a magnetic field, the degeneracy of spins is lifted, and the spin of the local level is along the field direction. As a result, the singlet-triplet representation is no longer suitable and all the plateaus become multiples of $0.5(2e^2/h)$ due to the splitting of spin subbands.

In summary, we demonstrate that a combination of anti-resonance of the singlet channel and Kondo physics provides a satisfying account of basic features associated with the "0.7 anomaly" in quantum point contacts.

CHAPTER 5

Numerical Renormalization Group Method

ABSTRACT: Wilson's numerical renormalization group method is used to calculate the spectrum function, which represent the strength of scattering between iteration electrons and local impurity.

5.1 Anderson model

The Anderson Hamiltonian for a single impurity is

$$\begin{aligned} H &= \sum_k \epsilon_k a^\dagger_{k\sigma} a_{k\sigma} + \epsilon_d d^\dagger_\sigma d_\sigma \\ &\quad + \sum_k (V_k a^\dagger_{k\sigma} d_\sigma + V^*_k d^\dagger_\sigma a_{k\sigma}) \\ &\quad + U(d^\dagger_\uparrow d_\uparrow)(d^\dagger_\downarrow d_\downarrow) \end{aligned} \tag{5.1}$$

where ϵ_k is measured from Fermi energy and σ is spin index. $a_{k\sigma}$ and d_σ annihilate electrons at k-state and local impurity state with spin σ respectively. Repeated spin indeces are assumed to be summed over. $U > 0$ is the Coulomb repulsion between a pair of localized electrons and V_k describe the coupling between local impurity state and k state in conduction band.

Considering the conduction band extend in energy from $-D-\mu$ to $D-\mu$, where $2D$ is the width of conduction band and μ is the chemical potential. Because the impurity state is isotropic, from the selection rule, the local impurity will only coupled to the s-wave states in the conduction band, the k index in Eq. 5.1 can be replaced by a energy index ϵ and the sum should be replaced by integration in the continuum limits.

$$\begin{aligned} H &= \int_{-D-\mu}^{D-\mu} \epsilon d\epsilon a^\dagger_{\epsilon\sigma} a_{\epsilon\sigma} + \epsilon_d d^\dagger_\sigma d_\sigma \\ &\quad + \int_{-D-\mu}^{D-\mu} (\rho(\epsilon))^{\frac{1}{2}} d\epsilon (V(\epsilon) a^\dagger_{\epsilon\sigma} d_\sigma + V(\epsilon)^* d^\dagger_\sigma a_{\epsilon\sigma}) \\ &\quad + U(d^\dagger_\uparrow d_\uparrow)(d^\dagger_\downarrow d_\downarrow) \end{aligned} \tag{5.2}$$

where $\rho(\epsilon)$ is the one-electron density of state per spin. It is convenient to measure the energies relative to the band width $2D$ in terms of the variable $\epsilon \to \epsilon/D$ and operators

$c_{\epsilon\sigma} = \sqrt{D}a_{\epsilon\sigma}$ (to make $[c_{\epsilon\sigma}, c_{\epsilon'\sigma'}] = \delta_{\epsilon\epsilon'}\delta_{\sigma\sigma'}$). Now the Hamiltonian is rewritten as

$$\begin{aligned} H &= \int_{-1-\mu}^{1-\mu} \epsilon d\epsilon c^\dagger_{\epsilon\sigma} c_{\epsilon\sigma} + \epsilon_d d^\dagger_\sigma d_\sigma \\ &+ \int_{-1-\mu}^{1-\mu} (\rho(\epsilon)/D)^{\frac{1}{2}} d\epsilon (V(\epsilon) c^\dagger_{\epsilon\sigma} d_\sigma + V(\epsilon)^* d^\dagger_\sigma c_{\epsilon\sigma}) \\ &+ U(d^\dagger_\uparrow d_\uparrow)(d^\dagger_\downarrow d_\downarrow) \end{aligned} \tag{5.3}$$

Different from the previous Hamiltonian, the chemical potential in here is a dimensionless parameter, which relate to the ordinary chemical potential by $\mu \longrightarrow \mu/D$.

5.2 Logarithmic discretization

The key point to solve the above Hamiltonian is logarithmic discretization in the energy space. A parameter $\Lambda > 1$ is introduced to divided up the energy space $[-1-\mu, 1-\mu]$ into a series of intervals, as Fig. 5.1 shows. The nth interval is from $(1-\mu)\Lambda^{-(n+1)}$ to $(1-\mu)\Lambda^{-(n)}$ for positive energies or $(-1-\mu)\Lambda^{-(n)}$ to $(-1-\mu)\Lambda^{-(n+1)}$ for negative energies. One can define a complete set of orthonormal functions spanning the whole band by Fourier series in each of the intervals

$$\psi^{\pm}_{np}(\epsilon) = \begin{cases} \frac{\Lambda^{n/2}}{[(\pm 1-\mu)(1-\Lambda^{-1})]^{1/2}} e^{i\omega^{\pm}_n p\epsilon} \text{ if } \epsilon \text{ is in the nth positive (negative) interval} \\ 0 \text{ otherwise} \end{cases} \tag{5.4}$$

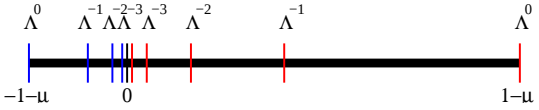

Figure 5.1. Logarithmic discretization of the conduction band. Energy zero is selected at Fermi energy and the top and bottom of the conduction band are at $-1-\mu$ and $1-\mu$, respectively.

Here n is the interval index, takes values $0, 1, 2, \cdots$, p is the Fourier harmonic index, takes all integer values from $-\infty$ to ∞, and $\pm$ denotes the intervals above the

Fermi energy (positive) or below the Fermi energy (negative). The Fourier frequency in the nth interval is

$$\omega_n^{\pm} = \frac{2\pi}{(\pm 1-\mu)(\Lambda^n - \Lambda^{n+1})} = \frac{2\pi\Lambda^n}{(1-\Lambda^{-1})(\pm 1-\mu)} \tag{5.5}$$

expand the operator $c_{\epsilon\sigma}$ in this complete basis

$$c_{\epsilon\sigma}(\epsilon) = \sum_{np}(a_{np\sigma}\psi_{np}^{+}(\epsilon) + b_{np\sigma}\psi_{np}^{-}(\epsilon)), \tag{5.6}$$

that one can express the Anderson Hamiltonian in terms of the discrete operators a_{np} and b_{np}.

$$\int_{-1-\mu}^{1-\mu} \epsilon d\epsilon c_{\epsilon\sigma}^{\dagger} c_{\epsilon\sigma} = \sum_{np} \epsilon_{a\,n}(a_{np\sigma}^{\dagger}a_{np\sigma} + \epsilon_{b\,m} b_{np\sigma}^{\dagger} b_{np\sigma}) + (1-\Lambda^{-1})O(1) \tag{5.7}$$

$$\int_{-1-\mu}^{1-\mu} d\epsilon c_{\epsilon\sigma} = (1-\Lambda^{-1})^{1/2} \sum_{n} \Lambda^{-n/2}(a_{n0\sigma} + b_{n0\sigma}), \tag{5.8}$$

where $\epsilon_{a\,n} = \int_{\epsilon_{n+1}^{+}}^{\epsilon_n^{+}} d\epsilon\epsilon\rho(\epsilon)/F_{an}^2$, $\epsilon_{b\,n} = \int_{\epsilon_n^{-}}^{\epsilon_{n+1}^{-}} d\epsilon\epsilon\rho(\epsilon)/F_{bn}^2$, with $F_{an}^2 = \int_{\epsilon_{n+1}^{+}}^{\epsilon_n^{+}} d\epsilon\rho(\epsilon)$, $F_{bn}^2 = \int_{\epsilon_n^{-}}^{\epsilon_{n+1}^{-}} d\epsilon\rho(\epsilon)$. $\epsilon_{a(b),n}$ can be well understood as the average energy within the nth interval. Ignoring the band structure and taking chemical potential at band center, $\epsilon_{a(b),n}$ can be solved analogically

$$\epsilon_{a(b),n} = \pm\frac{1}{2}(1+\Lambda^{-1})\Lambda^{-n} \tag{5.9}$$

From the Eq. 5.8, it is clear that the impurity only couples directly to the operators $a_{n0\sigma}$ and $b_{n0\sigma}$, and the operators $a_{np\sigma}$ and $b_{np\sigma}$ with $p \neq 0$ should only be considered in the second term of Eq. 5.7. Because of the factor $1-\Lambda^{-1}$ in front of this term, this coupling is small if Λ is close to 1.

5.3 Onion model

As the first approximation, the terms with $p \neq 0$ will be ignored. Calculations be various authors has confirmed that this is a good approximation even for Λ as

large as 3. The resulting Hamiltonian after approximation is

$$\begin{aligned} H &= \sum_{n=0}^{\infty}(\epsilon_{a\,n} a^{\dagger}_{n\sigma} a_{n\sigma} + \epsilon_{b\,n} b^{\dagger}_{n\sigma} b_{n\sigma}) \\ &\quad +\epsilon_d d^{\dagger}_{\sigma} d_{\sigma} + \Gamma(f^{\dagger}_{0\sigma} d_{\sigma} + d^{\dagger}_{\sigma} f_{0\sigma}) + U(d^{\dagger}_{\uparrow} d_{\uparrow})(d^{\dagger}_{\downarrow} d_{\downarrow}). \end{aligned} \tag{5.10}$$

where Γ is the impurity level width which is proportional to the coupling V. f_0 is a new operator defined as

$$\begin{aligned} \Gamma f_0 &= \int_{-1-\mu}^{1-\mu} (\rho(\epsilon)/D)^{\frac{1}{2}} (V(\epsilon) c_{\epsilon} d\epsilon \\ &= \Gamma \sum_{n} (u_{0,n} a_{n,\sigma} + v_{0,n} b_{n,\sigma}), \end{aligned} \tag{5.11}$$

where $u_{0,n} = F_{an}/F$ and $v_{0,n} = F_{bn}/F$. Here, the coupling $V(\epsilon)$ is chosen as a constant and $F^2 = \int_{-(1-\mu)}^{1-\mu} d\epsilon \rho(\epsilon)$.

In the Eq. 5.10, the impurity is only coupled to the operator f_0, which is essentially conduction electron field operator at the impurity site. It is convenient to transform from the basis (a_n, b_n) to a new set of orthonormal basis (f_m) with f_0 continuing to be given by Eq. 5.11. Because the kinetic energy of conduction electrons is diagonal in the set (a_n, b_n), the Hamiltonian representing in the new basis (f_m) will couple f_ms to one another. The best one can do is to choose such a transformation so that the operators f_m only exhibit nearest neighbor coupling.

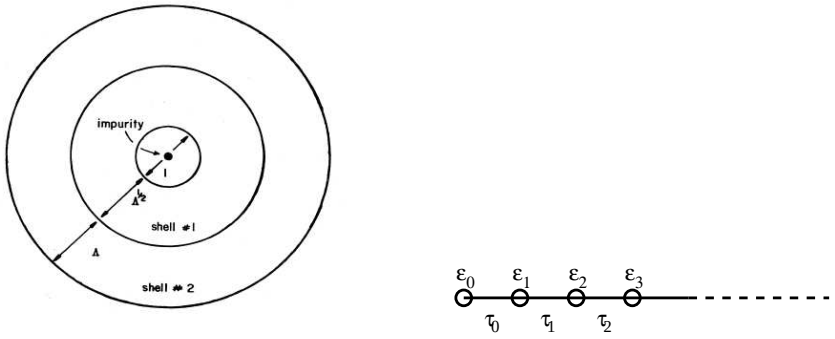

(a) (b)

Figure 5.2. Onion shell: Each shell represent a conduction state which only coupled with the nearest neighboring two shells. Only the center shell will couple with the local impurity state. The latter figure illustrates the corresponding Hamiltonian.

Lanczos recursion method is a good candidate to generate such a series of basis f_m. Starting form the initial state f_0, the next state is generate by

$$\epsilon_1|f_1>=H|f_0>-<f_0|H|f_0>|f_0>. \tag{5.12}$$

Repeating this process and make sure in each step the new generated state is orthogonal to the all previous states, one can finally get a new set of orthonormal basis (f_m). The Hamiltonian for the conduction electrons representing in this basis becomes

$$H_c=\sum_{n=0}^{\infty}\Lambda^{-n/2}[e_n f^{\dagger}_{n,\sigma}f_{n,\sigma}+t_n(f^{\dagger}_{n,\sigma}f_{n-1,\sigma}+\text{H.c.})], \tag{5.13}$$

where e_n and t_n are obtained from the re-orthogonalization in iteration steps of the Lanczos method. As has been discussed by many authors [59], the hopping coefficients and the on-site energies in the tridiagonal Hamiltonian matrix decrease as fast as $\Lambda^{-n/2}$ for large n.

5.4 Iterative diagonalization

The Wilson onion model is built up by adopting states f_n's as a basis for the single-electron states in the conduction band. The Anderson Hamiltonian can be rewritten as the limit of a series of Hamiltonians H_N [59]. One define a sequence of Hamiltonian H_N as following

$$\begin{aligned} H_N &= \Lambda^{(N-1)/2}[\sum_{n=0}^{N-1}\{\Lambda^{-n/2}t_n(f^\dagger_{n\sigma}f_{n-1\sigma}+f^\dagger_{n-1\sigma}f_{n\sigma})+e_nf^\dagger_{n,\sigma}f_{n,\sigma}\} \\ &\quad +\epsilon_d d^\dagger_\sigma d_\sigma+\Gamma(f^\dagger_{0\sigma}d_\sigma+d^\dagger_\sigma f_{0\sigma})+U(d^\dagger_\uparrow d_\uparrow)(d^\dagger_\downarrow d_\downarrow) \end{aligned} \tag{5.14}$$

The Anderson Hamiltonion can be recovered as the limit

$$H_A = lim_{N\to\infty} D\Lambda^{-(N-1)/2}H_N \tag{5.15}$$

The $\Lambda^{-(N-1)/2}$ factor in Eq. 5.14 is introduced so that the lowest energy scale in H_N, which is the coefficient of $f^\dagger_{N-1\sigma}f_{N\sigma}$, be of order of unit.

This series of Hamiltonions H_N have the following recursion relation,

$$H_N = \Lambda^{1/2}H_{N-1}+e_Nf^\dagger_{N,\sigma}f_{N,\sigma}+t_{N-1}(f^\dagger_{N,\sigma}f_{N-1,\sigma}+\text{H. C.})-E_{G,n}. \tag{5.16}$$

where $E_{G,n}$ is chosen so that the ground state energy of H_n is zero. The Hamiltonian H_0 describes the atomic limit of the impurity problem,

$$H_0 = \epsilon_d n_d + Un_\uparrow n_\downarrow \tag{5.17}$$

and H_1 includes the impurity and the conduction state coupling directly with it,

$$H_1 = \Lambda^{1/2}H_0+e_0f^\dagger_{0,\sigma}f_{0,\sigma}+t_0(f^\dagger_{0,\sigma}d_\sigma+\text{H.c.})-E_{G,1}. \tag{5.18}$$

This sequence of Hamiltonians H_N can be solved iteratively on the many-body basis [59, 60] so that the eigenenergies of H_{n+1} is same as those of H_n. The eigen-wavefunctions solved in H_{n-1} are used to construct the basis for H_n. At each step, the

Hamiltonian is rescaled by a factor $\Lambda^{1/2}$ so that the smallest energy scale of all H_n's is always in the order of 1. A further treatment is required because the dimension of the many-body basis exponentially expands in the iteration. Due to the low energy excitation nature of the Kondo problem, only M eigen states with the lowest eigen energies are retained. As the iteration going on, the eigensolutions will approach a fixed point, at which the spectrum of H_{n-2} is identical to that of H_n.

5.5 Numerical results

As the Fig. 5.1 shows, we first divide the conduction band into 48 bins, half below Fermi energy and half above the Fermi surface. Λ is 2.8 in the calculation. Fermi surface is taken at energy zero point. After Logarithmic discretization of the Anderson Hamiltonian, Lanczos method is used to generate the onion model. During Renormalization recursion, as more as $M = 1600$ many-body wavefunction is remained.

In the Fig. 5.3 and 5.4 we plot the rescaled e and t as a function of recursion N. the parameters are $\epsilon_d = -0.1t_0$, $U = 0.2t_0$, $\mu =$, where $4t_0$ is the conduction width. As increasing Fermi surface in the conduction band, the effective energy barrel for e seems decrease, while the effective hopping t saturate to a higher values.

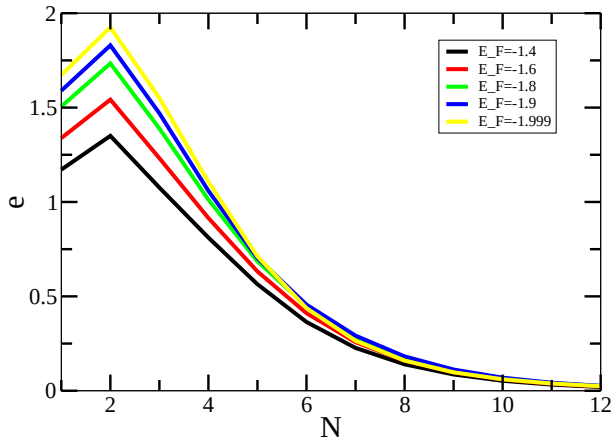

Figure 5.3. rescaled e as a function of recursion N..

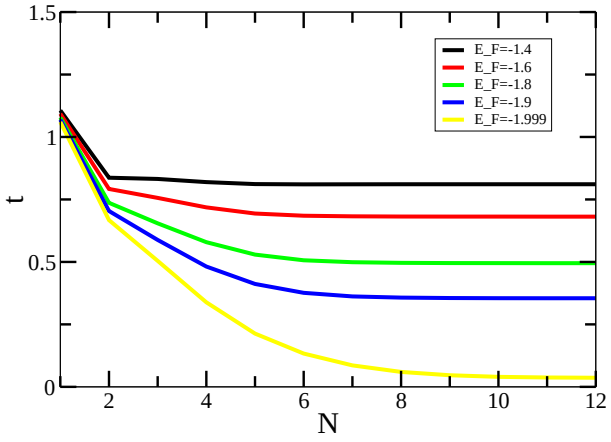

Figure 5.4. Rescaled t as a function of recursion N

We study the spectral density $\rho^n_\sigma(\omega, T)$ associated with the Green function defined as $G^n_\sigma(\omega, T) = \langle\langle d_\sigma; d^\dagger_\sigma \rangle\rangle$ in the nth iteration,

$$\rho^n(\omega, T) = \frac{1}{Z_n(\beta)} \sum_{p,p'} |d^n_{p,p'}|^2 (e^{-\beta E^n_p} + e^{-\beta E^n_{p'}}) \delta(\beta - E^n_{p'} + E^n_p), \tag{5.19}$$

where $Z_n(\beta)$ with $\beta \equiv 1/(k_B T)$ is the partition function and $d^n_{p,p'}$ are the matrix elements of the local impurity operator d in the representation of eigen-wavefunctions of the nth step. The values of $d^n_{p,p'}$ can be evaluated recursively in the iteration [58].

In Fig. 5.5, we plot the spectral density $\rho^n(\omega, T)$ as a function of ω for various recursion n, or in another word for various temperature T. Higher n correspond to lower temperature. Decreasing temperature, the peak for the spectral density $\rho^n(\omega, T)$ at $\omega = 0$ will become higher and sharper, indicating the emergence of density of state peak at Fermi surface. This result is in good agreement with the result by other authors. The chemical potentials in this figure is $-1.982 t_0$, which is relatively high.

We also calculate the spectral density $\rho^n(\omega, T)$ at low carrier density limit. In the Fig. 5.6, we plot $\rho^n(\omega, T)$. All parameters are same as those in the Fig. 5.5, except the chemical potential is $-1.9998 t_0$.

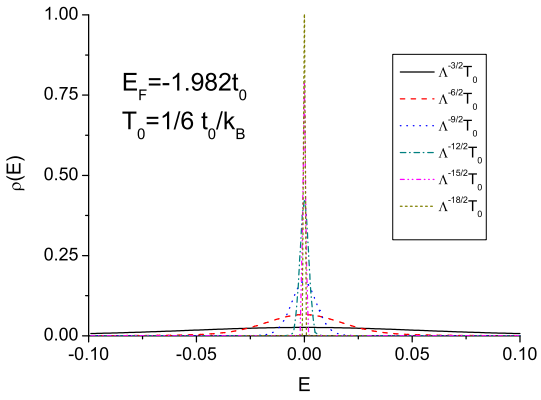

Figure 5.5. The spectral density $\rho^n(\omega, T)$ as a function of ω for various recursion n. The chemical potential is taken at $-1.982t_0$

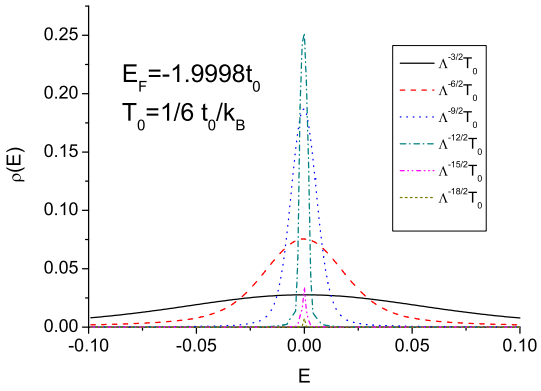

Figure 5.6. The spectral density $\rho^n(\omega, T)$ as a function of ω for various recursion n. The chemical potential is $\mu = -1.9998t_0$.

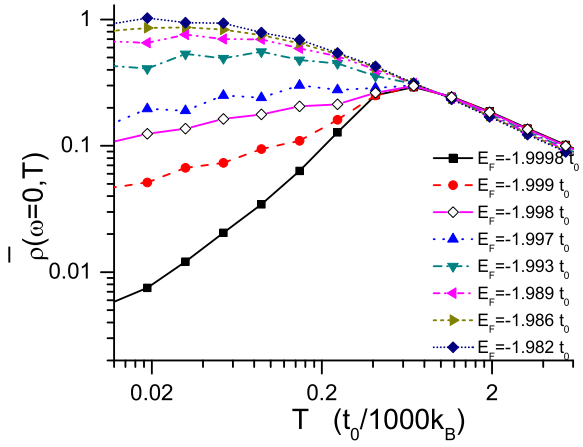

Figure 5.7. The spectrum at Fermi furface as a function of T. The energy of the local state is below the Fermi level by $10^{-3}t_0$ and the Coulomb repulsion U is $2 \times 10^{-3}t_0$. The hopping integral $t' = 0.02t_0$.

The spectral density in the Fig. 5.6 shows quit different behavior against that in the Fig. 5.5. In the Fig. 5.5, the spectral density $\rho^n(\omega = 0, T)$ increase with lowing temperature, indicate the Kondo singlet is favorate at low temperature. But in the Fig. 5.6, we have inverse property, the spectral density $\rho^n(\omega = 0, T)$ first increase with lowing temperature in the region $[\Lambda^{-6}T_0, T_0]$, indicate the emergence of Kondo effect at relative low temperature. But further decreasing temperature, the $\rho^n(\omega = 0, T)$ does not keep increasing as that in the Fig. 5.5. Instead, it will decrease and goes down to zero, indicate the disappearance of Kondo singlet at low temperature. This is a quite unusual behavior and never be reported before to our knowledge. We will discuss the physics behind this behavior later.

In 5.7, we plot the spectrum at Fermi furface verse T for different values of the Fermi level. The curves reflect the behavior of the SD near the Fermi level. For higher Fermi level the SD exhibits the usual $1 - \alpha T^2$ behavior of the ordinary Kondo effect. By lowering the Fermi level, the SD begins to decrease with decreasing temperature,

resulting in a peak. In the RG calculation the contributions to the SD are from the layers of the onion with statistical weights exponentially decaying from the outer to the inner. The states in the outer layers are more extended, the kinetic energy will be enhanced if an electron is transferred from these layers to the local impurity. This prohibits the access of these layers to the impurity in the case of low Fermi level. In decreasing the temperature, the number of onion layers increases. For low Fermi level, the outer layers newly added cease to contribute to the SD after a temperature, as the electrons in these layers can not access the impurity state. Thus, the SD will begin to decrease as the statistical weights of the inner layers $e^{-T_A/(2T)}$, where T_A corresponds to a characteristic energy associated with the many-body correlation.

This abnormal temperature dependence of SD can also be understood in a more physical way. As the Kondo effect emerging, the conduction electrons tend to localize around impurity state forming the Kondo cloud to screen the impurity. But as the Fermi surface is near the band bottom, the extensive nature of the states at the Fermi surface will prohibit the formation of the Kondo cloud.

5.6 Going back to QPC

As we keep going to discuss the relation between Kondo effect and "0.7" anomaly observed in Quantum Point Contact(QPC), we should first mention the difference of Kondo physics in QPC and Quantum Dot. In Quantum dot, the quantum dot is geometric larger than the size of typical Kondo cloud. As the electrons is moving from source to drain, it does not coupled to the impurity on the dot but exchange with the conduction electrons forming Kondo cloud. The state caused by Kondo effect on the Fermi surface provide a extra channel so that Kondo effect in quantum dot will enhance the tunneling. But in Quantum Point Contact, the contact is so small that conduction electron does not exchange with conduction electrons in Kondo singlet but coupled to the impurity directly. This case is more like the magnetic impurity

doping in metal. The Kondo effect in this case will provide a extra scattering so that Kondo effect enhance the resistivity.

For low E_F the conductance is $G(T) \approx \frac{2e^2}{h}\left(1 - \frac{a^2 e^{-T_A/T}}{2t_0\Delta^3}\right)$. For higher temperatures we have $\bar{t'}_{0,0} > t'_{\text{thre}}$ and $G(T) \approx 0.75\frac{2e^2}{h}$, and for lower temperatures $\bar{t'}_{0,0} < t'_{\text{thre}}$ and $G(T) \approx \frac{2e^2}{h}$. Thus, we reproduce the transition from full quantization of the conductance to $\frac{3}{4}$ quantization. The temperature dependence of the conductance in this transition is in agreement with the experiments of QPC [53]. In fact, if a Kondo cloud was formed, its size would be $\hbar v_F/k_B T_K$, with v_F being the Fermi velocity that approaching zero in the present case. This would enhance the energy of the Kondo cloud due to the size effect. Thus, at very low temperatures the Kondo cloud collapses and the accessibility of the singlet channel to the local state is reduced.

Bibliography

[1]T. Kasuya and A. Yanase, Rev. Mod Physics, 40, 684 (1968).

[2]H. Munekata, H. Ohno, S. Von Molnar, A. Segmuller, L. L. Chang, and L. Esaki, Phys. Rev. Lett., 63, 1849 (1989).

[3]H. Ohno, Science, 281, 951 (1998).

[4]T. Dietl, H. Ohno, F. Matsukura, Phys. Rev. B, 63, 195205 (2001).

[5]M. Johnson, R. H. Silsbee, Phys. Rev. Lett., 55, 1790 (1985).

[6]G. Schmidt, D. Ferrand, L. W. Molenkamp, A. T. Filip, B. J. van Wees, Phys. Rev. B, 62, R4790 (2000).

[7]J. A. Gaj, R. Planel, G. Fishman, Solid State Comm. 29, 435 (1979).

[8]See *C*olossal magnetoresistive Oxides, ed. by Y. Tokura, (Gordon and Breach Sciences Publishers, 2000).

[9]P. Schiffer, A. P. Ramirez, W. Bao, and S. W. Cheong, Phys. Rev. Lett. **7**5, 5144 (1995).

[10]M. Uehara, S. Mori, C. H. Chen, and S. W. Cheong, Nature(London) **3**99, 560 (1999).

[11]N.A. Babushkina *e*t al. Phys. Rev. B **6**2, R6081 (2000).

[12]G.M. Zhao, H. Keller, J. Hofer, A. Shengelaya, and K.A. Müller, Solid State Commun. **1**04, 57 (1997); M.R. Ibarra et al., Phys. Rev. B **5**7, 7446 (1998).

[13]G. Allodi *e*t al., Phys. Rev. B **5**6, 6036 (1997); Hennion *e*t al., Phys. Rev. Lett. 81, 1957 (1998).

[14]A. Moreo, S. Yunoki and E. Dagotto, Science 283, 2034 (1999) and references therein.

[15]E. Marinari *e*t al., Phys. Rev. B **6**2, 4999 (2000).

[16]To simplify our problem, we just take two possible orientations for magnetization of ferromagnetic domains in the mixtures.

[17]B. Derrida and J. Vannimenus J. Phys. A: Math. Gen. **1**5, L557-L564 (1982).

[18]M. Suzuki, *Q*uantum Monte Carlo Methods in Condensed Matter Physics, (World Scientific Publishing Co. Pte. Ltd.).

[19]See, for example, M. Plischke and B. Bergersen, *E*quilibrium Statistical Physics, (World Scientific, 1989).

[20]A. Bunde and S. Havlin, *F*ractal and disordered systems (Springer-Verlag Berlin Heidelberg New York 1996).

[21]B. I. Shklovskii and A. L. Efros, *E*lectronic properties of doped semiconductors, (Springer-Verlag Berlin Heidelberg New York Tokyo 1984).

[22]See, for example, E. L. Nagaev, *P*hysics of Magnetic Semiconductors, (Moscow, Mir Publ, 1979).

[23]G.M. Zhao, Phys. Rev. B**6**2, 11639 (2000).

[24]J.R. Shi and X.C. Xie, Phys. Rev. B**6**3, 045123 (2001); J.R. Shi, S. He, and X.C. Xie, cond-matt/9904393.

[25]E. Abrahams, P. W. Anderson, D. C. Licciardello, and T. V. Ramakrishnan, Phys. Rev. Lett. **4**2, 673 (1979).

[26]S. V. Kravchenko *e*t. al. Phys. Rev. B **5**0, 8039 (1994).

[27]S. He and X.C. Xie, Phys. Rev. Lett. **80**, 3324 (1998).

[28]Y. Meir, Phys. Rev. Lett. **83**, 3506 (1999).

[29]S. Das Sarma and E.H. Hwang, Phys. Rev. Lett. **84**, 5596 (2000).

[30]B.L. Altshuler and D.L. Maslov, Phys. Rev. Lett. **82**, 145 (1999).

[31]M.Y. Simmons *e*t.al., Phys. Rev. Lett. **84**, 2489 (2000); G. Brunthaler *e*t.al., Phys. Rev. Lett. **87**, 096802 (2001).

[32]J. Shi, S. He and X.C. Xie, Phys. Rev. B **6**0, R13950 (1999); J. Shi and X.C. Xie, Phys. Rev. Lett. **88**, 086401 (2002).

[33]N. F. Mott, J. Non-Cryst. Solids, **1**, 1 (1968).

[34]D.J. Thouless, Phys. Rev. Lett. **39**, 1167 (1977); Solid State Comm. **34**, 683 (1980).

[35]M. Kukuchi, J. Non-Cryst. Soilds, **59**, 25 (1983).

[36]P. Thomas, J. Non-Crystalline Solids **77**, 121 (1985).

[37]T. Lieberherr and H. Beck, Helvetica Physica Acta, **62**, 351 (1989).

[38]P. Mohanty, E. M. Q. Jariwala, and R. A. Webb, Phys. Rev. Lett. **78**, 3366 (1997).

[39]Yong-Jian Xiong and Shi-Jie Xiong, Phys. Rev. B **65**, 201302(R) (2002).

[40]E. Schrödinger, *S*tatistical Thermodynamics, Cambridge, Cambridge 1952.

[41]B.J. van Wees *e*t al., Phys. Rev. Lett. **6**0, 848 (1988).

[42]D.A. Wharam *e*t al., J. Phys. C **2**1, L209 (1988).

[43]K.J. Thomas *e*t al., Phys. Rev. Lett. **7**7, 135 (1996).

[44]K.J. Thomas *e*t al., Phys. Rev. B **5**8, 4846 (1998).

[45]A. Kristensen *e*t al., Physica (Amsterdam) **2**49B - **2**51B, 180 (1998).

[46]K.S. Pyshkin *e*t al., Phys. Rev. B **6**2, 15842 (2000).

[47]V.V. Flambaum and M. Yu. Kuchiev, Phys. Rev. B **6**1, R7869 (2000).

[48]Y. Meir, K. Hirose, and N.S. Wingreen, Phys. Rev. Lett. **8**9, 196802 (2002); *i*bid. **9**0, 026804 (2003).

[49]T.A. Costi, Phys. Rev. Lett. **8**5, 1504 (2000).

[50]D. Bercioux, M. Governale, V. Cataudella, and V. M. Ramaglia, Phys. Rev. Lett. **9**3, 056802 (2004).

[51]Shi-Jie Xiong and Ye Xiong, Phys. Rev. Lett. **8**3, 1407 (1999).

[52]C. Gonzalez-Buxton and K. Ingersent, Phys. Rev. B **5**7 14254 (1998).

[53]A. Kristensen *e*t al., Phys. Rev. B **6**2, 10950 (2000).

[54]S.M. Cronenwett *e*t al., Phys. Rev. Lett. **8**8, 226805 (2002).

[55]D. Goldhaber-Gordon *e*t al., Phys. Rev. Lett. **8**1, 5225 (1998).

[56]X.R. Wang, Yupeng Wang, and Z.Z. Sun, Phys. Rev. **B**65, 193402 (2002).

[57]T.K. Ng and P.A. Lee, Phys. Rev. Lett. **6**1, 1768 (1988); L.I. Glazman and M.E. Raikh, JETP Lett. **4**7, 452 (1988); Y. Meir, N.S. Wingreen, P.A. Lee, Phys. Rev. Lett. **7**0, 2601 (1993).

[58]T. A. Costits, A. C. Hewsont and V. ZlatiE, J. Phys. Condens. Matter., **6**, 2519 (1994).

[59]K. G. Wilson, Rev. Mod. Phys., **4**7, 773 (1975).

[60]H. Krishnamurthy, J. W. Wilkins, and K. G. Wilson, Phys. Rev. B **2**1, 1003 (1980); **2**1, 1044 (1980).

VITA

YE XIONG

Candidate for the Degree of

DOCTOR OF PHILOSOPHY

Thesis: CHARGE AND SPIN TRANSPORT IN COMPLEX SYSTEMS ASSOCIATED WITH SPINTRONICS.

Major Field: PHYSICS

Biographical:

Personal Data: Born on January 13, 1977

Education: Graduated from Jinling High School, Najing, China in May 1994; received Bachelor of Science in Physics from Nanjing University in May 1998; received Master of Science in Physics from Oklahoma State University in May 2005. Completed the requirements for the Doctor of Philosophy with a major in Physics at Oklahoma State University in December 2005.

Experience:

Professional Memberships:

Name: YE XIONG Date of Degree: December, 2005

Institution: Oklahoma State University Location: Stillwater, Oklahoma

Title of Study: CHARGE AND SPIN TRANSPORT IN COMPLEX SYSTEMS ASSOCIATED WITH SPINTRONICS.

Pages in Study: 66 Candidate for the Degree of Doctor of Philosophy

Major Field: PHYSICS

Scope and Method of Study: The purpose of this study was to explore charge and spin transport in several complex systems associated with spintronics. A distinct conductivity exponent observed at the percolation transition point in some colossal magnetoresistance (CMR) materials was studied by a realspace-renormalization method and numerical calculations. We also investigated the low temperature transport properties in a two dimensional electronic system coupled with phonons. After this, we studied spin entanglement effect between itinerant and localized electrons in a short one dimensional chain with low Fermi energy.

Findings and Conclusions: The distinct conductivity exponent could be understood by the concurrent occurrence of percolation transition and magnetic transition. The observation of exponent variance by a factor of 3 with or without external magnetic field could be well explained in our study. As to the second problem, we found the distribution of phonons near zero temperature departed from the Boson distribution because the entangled states were preferred from the energy point of view. This led to the low-temperature saturation of the variable range hopping of electrons and the existence of a metal-like behavior in two dimensions. Finally, in Quantum Point Contacts (QPC), as long as the entanglement between itinerant and localized electrons was maintained, a 3/4 quantum conductance occurred due to the blockade for the singlet state but not on the triplets. This would result in an observation of conductance near "0.7". We found that this blockade effect was complete as the effective coupling between itinerate and localized electrons exceeding a threshold. The many-body correlation of electrons near the band edge reduced this accessibility at low temperature and caused specific temperature dependence of the conductance. These results provided a natural explanation for the "0.7 anomaly" in QPC.

ADVISER'S APPROVAL: _____